Revised version submitted to *Cement and Concrete Research*

Influence of curing temperature on belite cement hydration: a comparative study with Portland cement

Shiva Shirani[1], Ana Cuesta[1], Alejandro Morales-Cantero[1], Angeles G. De la Torre[1], Margie P. Olbinado[2], Miguel A. G. Aranda[1]*

[1]*Departamento de Química Inorgánica, Cristalografía y Mineralogía, Universidad de Málaga, Málaga, 29071, Spain.*

[2]*Paul Scherrer Institut, 5232 Villigen PSI, Switzerland*

** email: g_aranda@uma.es*

Abstract.

Belite cements (BCs) could be a more sustainable binder than Portland cements (PCs) but adequate knowledge of the hydration features has still to be built. In particular, the mild curing hydration temperature effects have been extensively studied for PCs but not for BCs. This research was triggered by a previous work reporting improved mechanical strengths of BCs at higher curing temperatures. Here, we report the hydration characteristics of a BC at 20, 40 and 60ºC and compared to those of a PC. We have corroborated previous findings and used a multi-technique approach including Rietveld phase analysis, thermal analysis, calorimetry, silicon MAS-NMR, mercury intrusion porosimetry and chiefly synchrotron X-ray microtomography, to thoroughly understand the different behavior. In a nutshell, the improved mechanical performances at mild curing temperatures for BCs are mainly due to a much larger belite degree of reaction, with lower porosity coarsening of belite cements also playing a role

Keywords: CO_2 footprint, C-S-H gel, microstructure, Rietveld analysis, synchrotron X-ray microtomography

1. Introduction.

Portland cements (PCs) world production is ~4 Gt/yr [1], being the main component for the fabrication of concretes [2], concrete likewise being the most used material after fresh water. In spite of its ubiquitous current usage, PC is a very environmentally contentious material. On average, for every ton of Portland clinker produced, 0.87 CO_2 tones are emitted to our atmosphere [3], that includes emissions from limestone decomposition and burning fuel. This translates into ~7% of the total anthropogenic CO_2 emissions [4]. Furthermore, its production releases gases and particles causing health damages [5]. There is a clear need to produce more sustainable concretes [6] with lower embodied carbon content and one way is to use cements with lower CO_2 and harmful gas footprints. However, it has been already identified that cement production is one of the most difficult industrial processes to decarbonize [7], hence modest advances are expected. One approach to (modestly but safely) reducing the CO_2 footprint of cements is to use active belite cements [4,8,9] where its environmental impact has been very recently estimated and compared to those of PCs and related alternative cement systems [10]. Belite cements and its activation have been very recently reviewed [11].

PCs are fabricated from clinker, obtained at ~1500 °C, by grinding with the setting regulator (i.e. calcium sulfates). A typical grey Portland clinker mineralogical composition is close to 65 wt% of C_3S (alite), 10 wt% of C_2S (belite), 15 wt% of C_4AF, 5 wt% of C_3A and ~5 wt% of other minor content phases, and hereafter the cement nomenclature [2] is followed for referring to the mineralogical phases. Belite cements (BCs) generally contain the same components but the amount of alite and belite are reversed. There are five motivation drivers for using BCs: (i) lower limestone demand with lower associated CO_2 emissions, ~8 %; (ii) slightly lower energy demand as the enthalpy of formation for alite and belite are -2931 and -2308 kJ/mol, respectively [10]; (iii) lower maximum kiln operating temperature, ~1300°C, which means additional lowering gas emissions from burning and less demanding kiln liner maintenance; (iv) lower temperature increase at early hydration age and chemical shrinkage which minimizes thermal cracking; and (v) last but not least, longer service life, due to the relatively larger fraction of C-S-H gel, the main hydration product of alite or belite, per unit volume of binder. However, there is currently one showstopper and two drawbacks for its general adoption. The showstopper is the lower reactivity of ordinary belite at room temperature with water, which results in slow early-age strength developments not meeting current standards. The drawbacks are the requirements of: i) more grinding energy; and ii) higher cooling velocities, which could result in slightly higher energy demand and higher investment.

This work was triggered by a previous report [12] where the compressive mechanical strength as a function of time and temperature for PCs and BCs were compared. It was reported that the compressive strength for a BC mortar at 28 days of hydration increased from 58 to 74 MPa, i.e. +28%, when the temperature raised from 20 to 70 ºC [12]. The corresponding values for a reference PC mortar declined from 58 to 46 MPa, or -21%. This tantalizing result was backed by an earlier investigation from the same authors [13]. This means that there is a conspicuous difference between BCs and PCs hydration behavior with temperature and its mechanistic explanation, including the microstructural differences, merited further research.

Relatively high temperatures in concretes may take place because of hot/warm weather, undissipated heat of hydration in large volumes, elevated temperature curing (e.g. steam), or a mix of these circumstances. The consequences of elevated temperatures in PC based concretes have been widely researched. The detrimental consequences of curing temperature on the mechanical strengths of PCs is known since more than 50 years [14]. The agreed main explanation for the observed behavior is a more heterogeneous distribution of hydration products leading to a coarser pore microstructure [15] with chemistry changes, like an evolution of ettringite towards AFm, also likely playing a role. This research showed that as temperature increases, there was a significant decrease in C-S-H bound water content and an increase of its apparent density [15]. A subsequent study focused on the density, Ca/Si (C/S) ratio and water/silicate (H/S) ratio in C-S-H gel with temperature [16]. It was concluded that:

i) the density varied from 1.90 to 2.10 g/cm^3; ii) the molar C/S ratio evolved from 1.90 to 1.71; and the H/S ratio changed from 5.1 to 2.7; when curing from 7 to 90 ºC, respectively. The main results being independently confirmed soon after by using ^{1}H nuclear magnetic resonance (NMR) relaxometry [17]. The increase in C-S-H mass density and its lower bounded water explains its more microporous nature which in turn contributes to justify the poorer mechanical performances of PC mortars and concretes at higher curing temperatures.

To the best of our knowledge, there is not report addressing the chemistry and microstructural changes with mild curing temperature in belite cements. Furthermore, although X-ray tomography is being widely used for cement-based materials [18–20], it has not been applied for studying the microstructural changes with curing temperature for PCs and BCs based binders. Hence, the goal of this investigation is to reproduce an earlier report indicating an increase of compressive mechanical strengths with temperature for belite cements, contrary to the well-known Portland cement behavior. Once/if confirmed, a detailed comparative study is carried out to have insights on the different behaviors by employing several techniques including high-resolution synchrotron X-ray microtomography.

2. Materials and Methods.

2.1. Starting material. Two industrially prepared cements have been used in this study. The Portland cement, CEM I 42.5 N, was provided by Cementos la Araña, FYM, (Malaga, Spain) which belongs to HeidelbergCement Group. The Belite cement, CEM I 42.5 N -like, was provided by Buzzi Unicem Sp (Italy) [21].

2.2. Pastes and mortars preparation. Pastes were prepared with a w/c (water-to-cement) mass constant ratio of 0.50. They were mechanically stirred for 90 s at 800 rpm, with 30 s pause, followed by another 90 s stirring at 800 rpm, to improve their homogeneity. Then, the pastes were poured into hermetically closed cylinders of polytetrafluoroethylene (PTFE), and rotated during the first 24h (16 rpm) at the selected temperature, 20ºC, 40ºC or 60ºC. Subsequently, cylinders were taken out and samples were kept submerged in water at the target temperature. At the selected ages, the hydration of the cement pastes was arrested. In order to do so, samples were manually ground, filtrated in a Whatman system and washed twice with isopropanol, and once with diethyl ether.

For the microtomographic experiment, pastes were directly loaded into glass capillaries of 0.50 mm of diameter with a syringe. The capillaries were sealed with grease (or by melting the tip at high temperature) to avoid any water loss. Capillaries were rotated during the first 24 hours of hydration.

Standard mortars with water/cement/sand mass ratios of 0.5/1/3 were mechanically homogenized according to EN196-1. Prisms with dimensions (40×40×160 mm^3) were cast and then de-aired in a jolting table (Model UTCM-0012, 3R, Montauban, France) with a total of 120 knocks. Moulds were half cast and knocked for 60 times for a better homogenization. After that, they were fully cast and other 60 knocks were carried out. The prisms were kept at 20, 40 or 60ºC and 99% RH during 24 hours. Subsequently, samples were demoulded and left within a water bath at the target temperatures until measurements were performed.

2.3. Analytical techniques.

2.3.1. Compressive and flexural strengths. Mechanical strength properties for the mortars were measured at room temperature in a press (Model Autotest 200/10 W, Ibertest, Madrid, Spain) according to EN196-1 and at a rate of 1.5 MPa·s^{-1}. PC and BC mortars at 20ºC were measured at 1, 2, 7, 28, 120 and 220 days and mortars at 40 and 60ºC just at 2 and 28 days of hydration. The reported flexural values are the average of three broken prisms. The reported compressive values are the average of the six broken specimens.

2.3.2. Textural characterization. The specific surface area for the cements was measured by multi-point N_2 adsorption with a BET (Brunauer–Emmett–Teller) (ASAP 2420, Micromeritics, USA) instrument. The fineness was measured in a Blaine fineness apparatus (Controls) according to UNE-

EN 196-6. The particle size distribution of the BC was measured by laser diffraction (Malvern MasterSizer S, UK) provided with a wet chamber. Powders were previously dispersed in isopropanol using an ultrasonic bath. The particle size distribution of the PC was measured by laser diffraction (Malvern Mastersizer 3000).

2.3.3. X-ray fluorescence (XRF) analysis. The elemental composition of the cements was measured by XRF using an ARL ADVANT'XP+ (Thermo Fisher) equipment at the SCAI–Universidad de Málaga.

2.3.4. Laboratory X-ray powder diffraction (LXRPD). X-ray powder diffraction data for all the samples were collected on a D8 ADVANCE (Bruker AXS) diffractometer (SCAI–Universidad de Málaga) in transmission geometry (θ/θ) which is equipped with a Johansson monochromator, using strictly monochromatic Mo-Kα_1 radiation, λ=0.7093 Å. Rietveld analysis was performed using the GSAS suite of programs and the EXPGUI graphic interface [22]. Final global optimized parameters were: background coefficients, zero-shift error, cell parameters, and peak shape parameters using a pseudo-Voigt function. The preferred orientation effect was observed for portlandite in the pastes and it was corrected by the March-Dollase approach [23]. The pastes were mixed with 20 wt% of quartz as an internal standard. The ACn (amorphous and crystalline non-determined) content was determined by the internal standard methodology [24]. This quartz was purchased from Alfa Aesar, 99.5% of purity, and it was sieved <125 μm, prior to the mixing. Its particle size distribution data are: $d_{v,10}$=1.0 μm, $d_{v,50}$=2.7 μm and $d_{v,90}$=6.6 μm.

2.3.5. Thermal analysis. analysis (TA). Differential thermal analysis (DTA) and thermogravimetric analysis (TGA) measurements for the pastes were performed in a SDT-Q600 analyzer from TA instruments (New Castle, DE). Two data sets were taken for every paste, a neat one and another for the hydration-arrested specimen. The temperature was varied from RT to 1000°C at a heating rate of 10 °C/min. Measurements were made in open platinum crucibles under synthetic air flow. The weighed loss from RT to 550 °C was assigned as chemically bounded water and the weighed loss from 550 to1000 °C was considered as CO_2. It is noted that the bound water content is slightly underestimated as the water released by the C-S-H gel above 550 ºC is not computed. These cements have limestone and hence it not straightforward to disentangle the two origins for the mass loss above 550ºC.

The free water content (FW), in wt%, was calculated for each paste using the total added water and the bounded water as reported in [25], according to equations(1) and (2):

$$BW = (BW_{TGA} \times CM) / (100\text{-}BW_{TGA}) \quad (1)$$

$$FW = TW - BW \quad (2)$$

where BW corresponds to bound water content, TW is the total nominal water content (in this case 33.3%, w/c=0.50), BW_{TGA} is the loss of mass measured from RT up to 550 °C from TGA curves of the pastes after hydration arresting and CM is the cement content (all the numbers in weight percentage).

2.3.6. Isothermal calorimetry. The study was performed in an eight channels Thermal Activity Monitor (TAM) instrument using glass ampoules. The paste preparation was carried out outside the calorimeter by mixing the cements with water and shaking for 1 minute manually and then for 1 minute with a vortex mixer. After homogenization, the pastes were inserted into the ampoules and then within the calorimeter. The heat flow curves were collected up to 7 days at the target temperatures, starting after 45 minutes of mixing for temperature stabilization.

2.3.7. MAS-NMR. ^{29}Si MAS-NMR (Magic Angle Spinning Nuclear Magnetic Resonance) spectra for selected pastes were recorded at RT on a Bruker AVIII HD 600 NMR spectrometer (field strength of 14.1 T) at 156.4 MHz. The chemical shift was referenced to an external solution of tetramethylsilane.

2.3.8. Mercury intrusion porosimetry (MIP). Pore entry size distributions were measured on cylindrical samples of dimensions: 1 cm of diameter and 1.5 cm of height. Two pieces of each paste were independently measured and the reported data are the average of the two traces which were very similar. The pastes were cured for 28 days following the procedure already described. Before MIP measurements, the hydration was arrested by sinking the pieces in isopropanol for 3 days. Then, the pastes were dried by gentle heating at 40ºC up to constant weight, which took about 5 days. In order to measure porosity in the range from 1 mm down to 4 nm (radius), a micromeritics AutoPore IV 9500 porosimeter (Micromeritics Instrument Corporation, Norcross - GA, US) was used. The pressure applied by the intrusion porosimeter ranged from 0 to 206 MPa in step mode. A constant contact angle of 140° was assumed for data evaluation [26]. It is acknowledged that C-S-H has a significant porosity in the pore diameter range 4-8 nm, which is not measured in this work

2.3.9. Synchrotron X-ray microtomography study. Microtomographic measurements were performed at the TOMCAT beamline at the Swiss Light Source (SLS) at Paul Scherrer Institut, Switzerland. All samples/capillaries were scanned with a monochromatic X-ray energy of 15 keV with a sample-to-detector distance of 5.5 mm, to obtain high contrast images. The image detector is composed of a 20-µm thick LuAG:Ce scintillator, a diffraction limited microscope optics, 20× objective, and a high-resolution CCD camera (pco.edge 5.5, PCO AG, Germany). The employed experimental setup resulted in an isotropic pixel size of 0.325 µm and a field of view of 0.8×0.7 mm (V×H), just large enough to image the full width of the capillaries, 0.5 mm of diameter (H). The exposure time for each frame was 200 ms. For each tomographic dataset, 1501 projections over 180º sample rotation were acquired which resulted in a total scan time of 5 min per sample for this high-resolution configuration. Phase retrieval of the projections was performed using the Paganin algorithm [27] and then tomographic reconstruction was carried out [28]. For each acquired tomogram, two full reconstructions were obtained with and without applying the Paganin algorithm. The reconstructions, without Paganin algorithm applied, are closed to the absorption values.

Data analysis, including phase component segmentation by manual thresholding, was carried out by using Dragonfly software (version 2020.2 for Windows^{TM}, Object Research Systems (ORS) Inc., Montreal, Canada). For the segmentation of the main components, a large Volume of Interest (VOI) of ~1×10^8 µm^3 size was selected for each sample. The Paganin reconstructed data were not post processed by denoising neither smoothing. The cylinder shape mask aligned for each dataset was chosen to leave out the capillary walls. The manual selection of the threshold values was carried out based on the shape of the greyscale histograms to differentiate between the three main components: i) porosity (air and water); ii) hydration products; and iii) unhydrated cement phases. There were valleys in the hydration products/unhydrated cement phases contributions and the thresholds were positioned in the valleys. For the pores/hydration products segmentation, and the absence of valleys between these contributions, the threshold choices were based on the shape of the greyscale voxel distribution, tangent-slope approach, see section 3.8.1 for more details. It is acknowledged that the manual histogram shape-based threshold choice may slightly affect the accuracy of the results of the segmentation.

3. Results and discussion.

3.1. Initial characterization of the anhydrous cements. Both cements were analyzed by LXRPD and XRF. Rietveld quantitative phase analyses and elemental analyses are reported in Tables S1 and S2, respectively. The textural properties are as important as the phase contents to interpret the reactivities. Therefore, a thorough textural characterization was carried out. Air permeabilities (Blaine values) were 369 and 502 m^2kg^{-1} for PC and BC, respectively. Fine milling of BCs is needed to enhance belite reactivity. Accordingly, the BET surface areas were 1.20(1) and 1.40(1) m^2g^{-1}. The PSDs are displayed in Fig. S1 with $d_{v,50}$ being 19.5 and 7.5 µm for PC and BC, respectively. Finally, average densities were 3.13 and 3.17 $g.cm^{-3}$ for PC and BC, respectively. The belite cement was employed in a previous study under oil well curing conditions and its textural properties were reported [29] but they are also given here for easy access to the information.

3.2. Mechanical strengths. The mechanical strength results are displayed in Fig. 1. At room temperature (panels *a* and *d*), the mechanical strengths increase with hydration time as expected, the PC values being higher than those of BC up to 3 months. As previously reported, for instance in [30,31], BC compressive strength surpassed that of PC above 100 days. A small drop in flexural strengths at later ages has been observed, see Fig. 1(d), which was not within the scope of this research and it deserves further investigation, if this behavior is confirmed.

As discussed in the introduction, the compressive and flexural strengths for PC stagnate and even decrease as hydration temperature increases. At 2 days of hydration, compressive and flexural strengths slightly increase at 40ºC and then slightly decrease at 60ºC, see Fig. 1b and e. This pattern is more evident at 28 days where the values decreases at 40 ºC and more pronounced at 60 ºC, see Fig. 1c and f. Conversely, the compressive strengths of BC at 2 and 28 days increase with temperature at 40 and even 60 ºC, see Fig. 1b and c. A similar behavior is displayed by the flexural strengths at 2 days, see Fig. 1e, although a slight decrease is observed at 28 days and 60ºC, see Fig. 1f. We speculate that the slight increase in the compressive strength for BC mortar at 28 days and 60ºC, accompanied by a decrease of the flexural strength, indicates that flexural strengths are much more sensitive to the pore coarsening that it takes place at this temperature, see below. However, the mechanistic understanding of this requires further investigation. In any case, the previous results [12,13] concerning compressive strengths are reproduced here, for a relatively different BC, where the compressive strengths increase +27% from 20 to 60ºC at 28 days for the BC mortar, meanwhile, and decrease -17% from 20 to 60ºC at 28 days for the PC mortar. It must be noted that the compressive strength differences at 28 days between the PC and BC mortars were +11, -5 and -13 MPa, for 20, 40 and 60 ºC, respectively, see Fig. 1c.

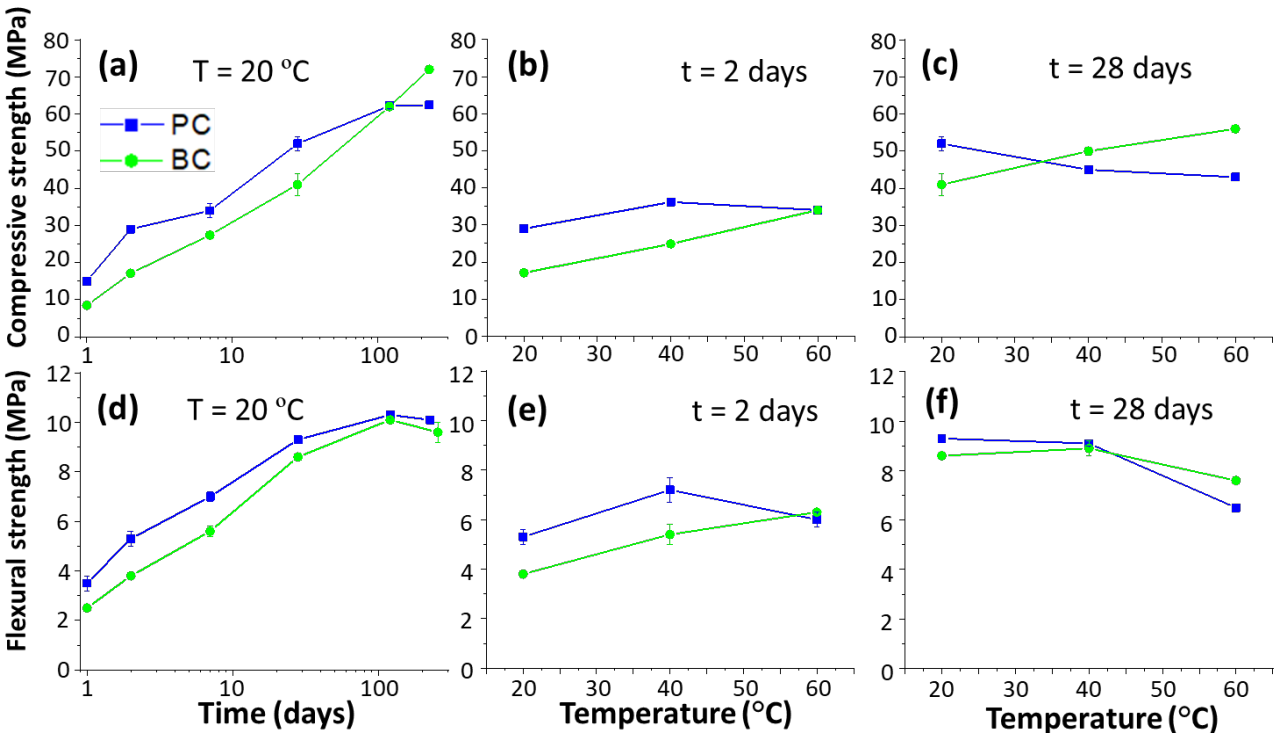

Fig. 1. Mechanical strength data for PC (blue) and BC (green) mortars. Time dependence of the compressive and flexural strengths: panels (a) and (d), respectively. Temperature dependence values (compressive) at 2 and 28 days, panels (b) and (c), respectively. Temperature dependence values (flexural) at 2 and 28 days, panels (e) and (f), respectively.

The remaining part of this paper is to report the findings on the hydration of BC at mild curing temperatures to help in the understanding of the different behaviors.

3.3. Laboratory X-ray powder diffraction study. The pastes were mixed with an internal standard (quartz) to determine the overall amorphous and crystalline-not-determined (ACn) content, [24,32].

Powder patterns were collected at 2 (3d for 20ºC), 7 and 28 days at the three studied temperatures for the two cements in the same conditions. Fig. 2 displays the raw powder patterns at 28 days and all hydration temperatures for an initial qualitative assessment.

The PC hydration behavior is fully in line with previous reports [15,16] where the main evolution with temperature was the destabilization of ettringite (AFt) and the formation of small amounts of calcium aluminate monosulfate (AFm) and katoite, mainly at 60ºC. On the other hand, BC presents a very interesting hydration behavior with temperature. It can be clearly seen that the hydration degree of belite at 28 days and 40 ºC is much larger than that at 20 ºC. This reaction degree further increases at 60ºC, see the right panel in Fig. 2. Additionally, and as expected, AFt decomposes and a much lower amount is observed at higher curing temperatures. This is accompanied by just a minor increase in the AFm content.

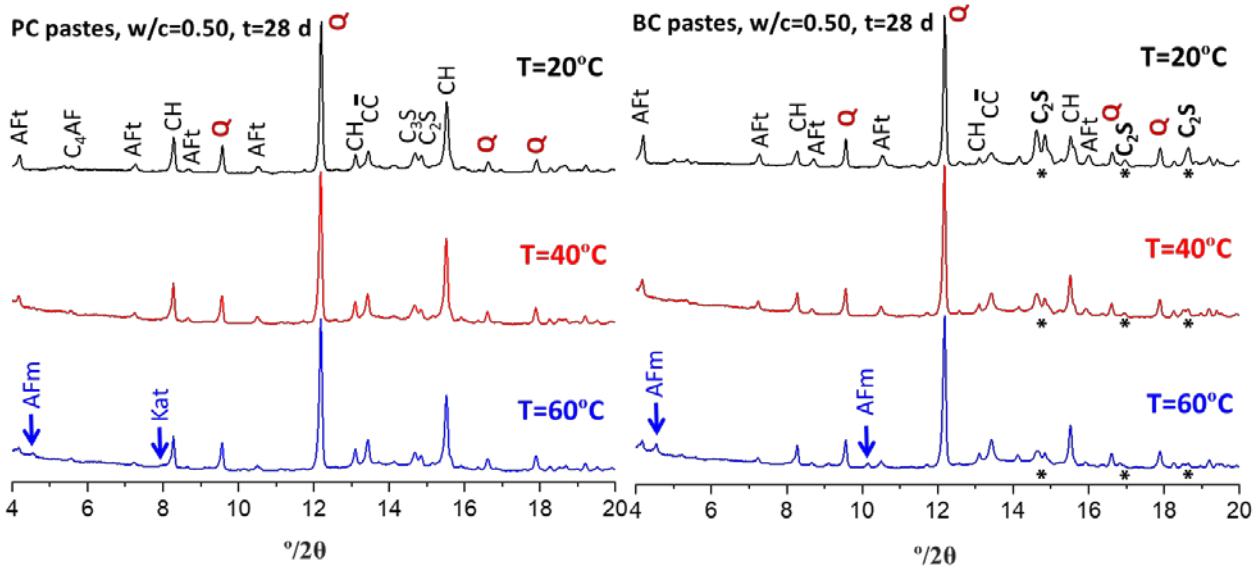

Fig. 2. Laboratory X-ray powder diffraction patterns (Mo-Kα_1, λ=0.71 Å) for PC (left) and BC (right) pastes as a function of hydrating temperature. The main peaks are labelled following the cement notation, including those of the internal standard (Q). The mains peaks for β-belite are highlighted (*) in the right panel for better visualization of its reactivity.

All LXRPD data have been analyzed by the Rietveld method, as described in the experimental section, in order to obtain the quantitative phase analyses (RQPA). The eighteen Rietveld plots, at every hydration time and temperature, are deposited in the Supplementary Information, Figs S2-S7. The resulting phase contents are summarized in Tables 1 and 2, for PC and BC pastes, respectively. The hydration degrees increased with time and temperature, as expected. For PC at 20ºC and 28 days, the reaction degree of C_3S and C_2S were 86 and 31%, respectively. At the same hydration time but at 40ºC, these values increased to 89 and 56%, respectively. Interestingly, at 60ºC, the hydration degree of C_3S stagnates at 88% but that of C_2S kept growing up to 71%. For BC at 20ºC and 28 days, the reaction degree of C_3S and C_2S were 85 and 54%, respectively. At 40ºC, these values augmented to 87 and 78%, respectively. Very interestingly, at 60ºC, the hydration degrees of C_3S and C_2S were 87 and 88%, respectively. It must be noted that at this temperature and hydration time, the reaction degree of belite is the same than that of alite within the errors of the measurements. The reaction degrees of tricalcium aluminate and tetracalcium aluminoferrate did not significantly change with temperature. Therefore, they are not further discussed here. The noticeable increase in the reactivity of belite with temperature (partly) explains the increase of compressive strengths showed by the belite cements. It must be noted that the higher reaction degree of C_2S at 20ºC and 28 days for BC, 54%, is higher than that of belite in PC in the same conditions, 31%, very likely because BC is ground to a finer value than PC, see subsection 3.1 above. It is also highlighted here that the quantitative data reported in Tables 1 and 2 were obtained for pastes and the mechanical strengths reported in Fig. 1

were determined for mortars. The possible (minor) impact of the sand in the early age hydration kinetics has not been studied by powder diffraction.

Concerning the hydrated phases, several observations deserved discussion. Firstly, and as previously reported [15,16,33], AFt contents decreased with temperature in both cement pastes, see Tables 1 and 2. However, at the same time, the crystalline AFm contents increased very little. Therefore, we concluded that the overall amorphous content, ACn, should contain a significant contribution from amorphous AFt/AFm at higher temperature or alternatively the liberated aluminum could be incorporated in the gel resulting in the formation of C-(A)-S-H. Secondly, there is not a crystalline iron-containing hydrated phase. Therefore, the hydration of C_4AF is assumed to yield amorphous Al- and Fe-siliceous hydrogarnet as previously reported [34]. This amorphous component is also included within our overall ACn content. Thirdly, katoite contents changed little and hence, their evolutions are not discussed here. Fourthly, the portlandite contents evolved as expected. For PC pastes at 28 days, the CH contents were 13.0, 13.4 and 11.6 wt% at 20, 40 and 60ºC, respectively. The corresponding values for BC were 4.3, 5.4 and 5.2 wt%, respectively. The portlandite contents increased at 40ºC because of the larger hydration degree of belite (and of alite but not at much lower extension). On the other hand, their contents decreased from 40 to 60ºC by 13 and 4% for PC and BC, respectively. This decrease is likely due to the reaction of portlandite with hydration phases like ettringite but further investigations are needed to firmly establish this point. Finally, it is noted that preferred orientation for CH was observed in the PC pastes but not in the BC ones. The March-Dollase preferred orientation correction values were 1.10-1.12, 1.12-1.14 and 1.14-1.16 for PC pastes hydrated at 20, 40 and 60ºC, respectively. The slightly larger values with hydrating temperature likely indicate slightly larger average sizes of CH crystals.

Table 1.
Mineralogical composition (wt%) for the Portland cement pastes at the studied temperatures determined by RQPA, including the ACn (overall amorphous content) and FW (free water).

		PC T=20ºC			PC T=40ºC			PC T=60ºC		
Phases	**t_0***	**3d**	**7d**	**28d**	**2d**	**7d**	**28d**	**2d**	**7d**	**28d**
C_3S#	32.1(3)	12.9(6)	8.9(5)	4.3(5)	7.8(5)	5.7(5)	3.5(3)	5.4(5)	4.8(5)	3.8(6)
β-$C_2S$$	7.3(7)	5.6(8)	5.0(4)	5.0(4)	6.3(6)	5.3(5)	3.2(6)	5.2(7)	3.2(4)	2.1(4)
C_4AF	6.4(4)	2.6(2)	2.4(2)	1.9(1)	2.3(1)	2.2(1)	1.9(2)	2.2(2)	1.9(2)	1.9(2)
C_3A	1.9(1)	1.5(1)	1.0(1)	0.5(1)	0.7(1)	0.6(1)	0.5(1)	0.6(1)	0.5(1)	0.5(1)
K_2SO_4	0.5(1)	0.6(2)	0.7(2)	0.6(2)	0.8(2)	0.6(2)	0.5(2)	0.8(2)	0.6(2)	0.5(2)
$C\overline{C}$	1.9(1)	3.3(2)	3.1(1)	1.9(1)	3.7(1)	2.6(1)	2.8(2)	2.4(2)	2.4(2)	2.7(2)
CH	-	9.6(3)	11.4(2)	13.0(2)	11.0(2)	12.3(2)	13.4(2)	11.2(2)	11.4(2)	11.6(2)
AFt	-	7.9(5)	8.6(4)	7.9(5)	5.1(4)	5.8(5)	5.5(5)	1.7(5)	2.2(5)	2.7(5)
AFm	-	--	-	0.4(1)	-	-	-	1.4(2)	0.8(2)	0.9(2)
Katoite	-	-	0.5(2)	0.7(2)	0.6(2)	0.7(2)	0.9(2)	0.8(2)	0.9(2)	1.0(2)
ACn	15.5	36.3	41.7	49.2	45.1	48.0	53.1	48.7	52.1	54.2
FW	33.3	19.7	16.7	**14.6**	16.6	16.4	**14.7**	19.6	19.2	**18.1**

* This binder also contains at t_0: 0.5 wt% of gypsum and 0.6 wt% of basanite. # The fits for alite in the hydrated pastes were carried out just with 100% M3 polymorph. $ The unit cell value for β-C_2S was 343.6(2) Å^3.

Table 2.
Mineralogical composition (wt%) for the belite cement pastes at the studied temperatures determined by RQPA, including the ACn and FW.

		BC T=20ºC			BC T=40ºC			BC T=60ºC		
Phases	**t_0***	**3d**	**7d**	**28d**	**2d**	**7d**	**28d**	**2d**	**7d**	**28d**
C_3S#	16.4(4)	6.2(5)	4.3(3)	3.8(2)	5.2(3)	4.2(4)	3.2(4)	3.6(5)	3.4(5)	3.3(5)
β-$C_2S$$	29.5(3)	29.0(4)	28.8(3)	20.1(4)	25.6(4)	19.4(5)	9.5(6)	19.5(7)	10.6(7)	5.4(8)
C_4AF	6.9(4)	4.8(4)	4.1(4)	1.8(3)	3.1(4)	2.8(4)	1.9(5)	3.4(5)	2.6(5)	1.9(6)
$C\bar{C}$	0.9(1)	1.1(1)	0.9(1)	1.3(1)	3.1(1)	3.4(1)	2.4(2)	2.1(2)	2.8(0)	2.8(0)
MgO	0.9(1)	0.8(1)	1.0(1)	0.9(1)	0.8(1)	0.9(1)	0.8(1)	1.1(1)	0.7(1)	0.5(1)
CH	-	3.1(2)	3.6(1)	4.3(2)	3.4(2)	4.1(2)	5.4(2)	4.5(2)	5.0(2)	5.2(3)
AFt	-	10.8(4)	9.2(4)	14.1(4)	7.5(4)	8.8(4)	8.3(5)	3.4(6)	4.0(5)	4.3(6)
AFm	-	0.5(1)	0.5(1)	1.9(2)	1.0(1)	1.1(2)	1.1(3)	4.1(3)	2.8(2)	2.6(3)
Katoite	-	-	0.5(1)	0.9(1)	0.7(2)	0.7(2)	0.8(2)	0.8(2)	0.9(2)	0.9(2)
ACn	9.1	22.2	27.3	37.0	29.9	37.7	52.4	37.7	50.0	58.1
FW	33.3	21.1	19.8	**13.9**	19.7	16.9	**14.2**	19.8	17.2	**15.0**

*This binder also contains: 0.7 wt% of C_3A, 1.3 wt% of $C_4A_3\bar{S}$ and 1.1 wt% of anhydrite. #At t_0, the alite content was 2.0 wt% of M3 and 14.4 wt% of M1. $ The unit cell value for β-C_2S was 344.7(1) Å^3, this larger volume could be due to the sulphur content of the clinker.

It is important to determine if the RQPA given in Tables 1 and 2 are close to the expected values based on the hydration reactions. We focus this comparison on C-S-H gel and portlandite as they are key components of the hydrated binder. The chemical reactions yielding C-S-H gel and portlandite are (3) and (4) [35]. Additionally, reaction (5) gives the reaction of belite and C_4AF to yield amorphous siliceous hydrogarnet and crystalline portlandite [36,37]. The reaction (6) is used in the case that all the C_2S has been consumed in reaction (5) and there is some C_4AF left.

$$Ca_3SiO_5 + 5.2\ H_2O \rightarrow (CaO)_{1.8}SiO_2(H_2O)_{4.0}\ (am.) + 1.2Ca(OH)_2\ (cryst.) \quad (3)$$

$$Ca_2SiO_5 + 4.2\ H_2O \rightarrow (CaO)_{1.8}SiO_2(H_2O)_{4.0}\ (am.) + 0.2Ca(OH)_2\ (cryst.) \quad (4)$$

$$0.84\ Ca_2SiO_4 + 0.5\ Ca_4Al_2Fe_2O_{10} + 5H_2O \rightarrow Ca_3AlFe(SiO_4)_{0.84}(OH)_{8.64}\ (am.) + 0.68Ca(OH)_2\ (cryst.) \quad (5)$$

$$0.84\ Ca_3SiO_5 + 0.5\ Ca_4Al_2Fe_2O_{10} + 5.84H_2O \rightarrow Ca_3AlFe(SiO_4)_{0.84}(OH)_{8.64}\ (am.) + 1.52Ca(OH)_2\ (cryst.) \quad (6)$$

From these hydration reactions, it is possible to calculate the expected portlandite and C-S-H contents. An example of this calculation is given in the Supplementary Information. The results are given in Table 3. As an example (PC-20ºC-28d), if the average Ca/Si ratio for C-S-H is assumed to be 1.70 instead of 1.80, the resulting theoretical CH content would be 12.6 wt% instead of 11.8 wt%. It can be seen that for Portlandite contents, the measured values by diffraction and thermal analysis, see below, are quite close to the expected values from the hydration of the cement phases in PC pastes at the three temperatures. Conversely, for BC pastes the measured values are significantly lower than the expected one. We partly justify this disagreement by the approximate nature of the used chemical reactions as for instance the Ca/Si ration in the C-S-H gel of belite binders could be higher leading to less crystalline portlandite. Additionally, BC contains 1.3 wt% of ye'elimite that hydrates with calcium sulphate to yield ettringite and ~0.7 wt% of nano-gibbsite, $Al(OH)_3$ gel. $Al(OH)_3$ is not stable in a portlandite rich environment and it could react helping to account for the disagreement between the expected and measured amounts of CH in the hydration of this BC. Furthermore, the final end of this aluminum is not clear as crystalline stratlingite is not detected. It could be possible that this

aluminum is incorporated in C-S-H gel yielding an Al-richer C-(A)-S-H. Aluminum is known to modify the C-S-H chemical nature and precipitation rate [38,39]. Furthermore, it has been recently reported that C_2S hydration degree strongly depends upon the aluminum environment [40]. Clearly, further research is needed to address the Al-role and the portlandite content disagreement. On the other hand, the comparison of the expected and indirectly measured C-S-H contents are better for BC than for PC pastes, see Table 3. In any case, taken into account the number of approximations carried out for these comparisons, the overall agreement is considered satisfactory and the trends are fully captured.

Table 3
Comparison of the measured portlandite (directly) and C-S-H gel (indirectly[$]) contents with the expected values (italics) from the hydration reactions (3) to (5) determined as detailed in the S.I.

Sample	***CH[#] /wt%***	**CH /wt% (RQPA)**	**CH /wt% (TA)**	***C-S-H[*] /wt%***	**C-S-H /wt% (RQPA)[$]**
PC-20ºC-28d	*11.8*	13.0	12.2	*28.0*	41.3
PC-40ºC-28d	*12.2*	13.4	13.0	*31.2*	44.0
PC-60ºC-28d	*12.2*	11.6	10.9	*32.4*	43.7
BC-20ºC-28d	*6.6*	4.3	5.0	*21.7*	28.0
BC-40ºC-28d	*7.8*	5.4	6.3	*36.7*	40.7
BC-60ºC-28d	*8.1*	5.2	6.5	*42.1*	44.4

[$] Calculated from the overall ACn values as described in the S.I.
[#] Expected values from the hydration of C_3S, C_2S and C_4AF.
[*] Expected values from the hydration of C_3S and C_2S.

3.4. Thermal analysis study. Fig. 3 displayed a compilation of the thermal analysis traces for all studied pastes (non-arrested hydration samples). The individual thermal analysis patterns for the eighteen samples are given in supplementary information, Figs. S8 to S13. The portlandite contents derived from these analyses, using the tangential method, are in full agreement with the values given above from the Rietveld quantitative phase analyses. The slight decrease in CH contents at 60 ºC for PC pastes are fully reproduced here. The larger CH content with temperature for BCs, due to the increased belite reactivity, is also evident through this technique, see Fig. 3. Furthermore, minor amounts of calcium carbonate are evident in the thermal traces, weight losses close to 650 ºC, which are coming mainly from the employed cements, see mineralogical compositions in the supporting information.

Free water contents were calculated as described in the experimental section and they were reported in Tables 1 and 2. In agreement with the advance of the hydration reactions, the FW decreases with the hydration time at every temperature. Importantly, and in agreement with previous publications [15–17], the FW content for the PC paste at 60ºC and 28 days, ~18 wt%, is larger than those obtained at 20 and 40ºC, ~15 wt%, despite the hydration degree being even slightly larger. This is fully compatible with denser C-S-H gel with lower highly-retained gel pore water content and hence, developing a larger fraction of capillary water. Even more importantly, as this is a totally novel result, the FW content for the BC pastes at 60ºC and 28 days, ~15 wt%, is only marginally larger than those shown at 20 and 40 ºC, ~14 wt%. Therefore, the coarsening of C-S-H gel with temperature for BC is much less important than that exhibited by PC which also helps to explain that BC showed better mechanical strength performances at relatively higher temperatures, see section 3.2 above.

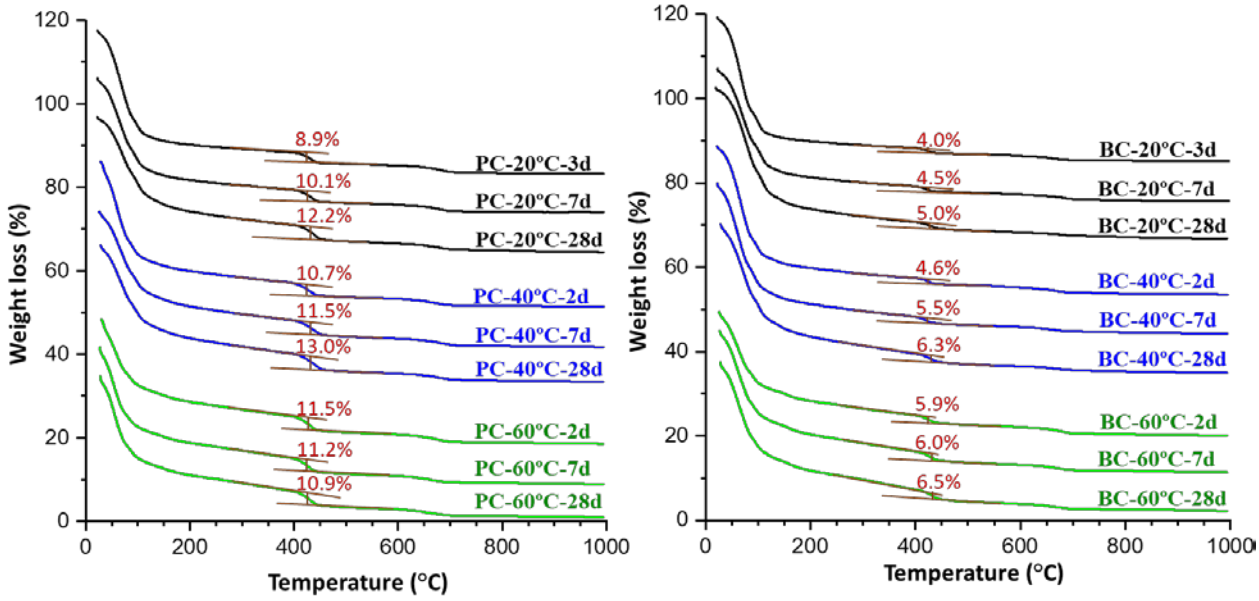

Fig. 3. Thermal analysis data as a function of time and temperature for Portland cement (left) and belite cement (right) pastes (non-hydration arrested samples). The traces have been displaced vertically for better visualization.

3.5. Calorimetric study. Fig. 4 displays the calorimetric study for the PC and BC pastes. The first peak in PC is due to alite hydration with a shoulder at a higher hydration time due to the aluminate hydration contribution. For BC, the first peak has two contributions, alite hydration and ye'elimite reaction to yield ettringite. As expected, the hydration of PC is accelerated at early ages by temperature and the maxima in the heat flow curve were measured at 11.0, 4.6 and 4.0 hours for 20, 40 and 60ºC, respectively. For BC cement paste, alite and ye'elimite hydrations are also accelerated by increasing temperature and the maxima took place at 17.4, 3.8 and 3.2 hours for 20, 40 and 60ºC, respectively. The cumulative heat developed for PC pastes at 7 days and 20, 40 and 60ºC were 310, 328 and 330 J/g, respectively, see Fig. 4 (b). Hence, an increase of 6.5% in the overall heat is measured when compared the data at 20 with 60ºC. The corresponding values for BC pastes were 211, 230 and 231 J/g, see Fig. 4 (d). Therefore, an increase of 9.5% in the cumulative heat is observed from 20 and 60ºC. It is noteworthy that the increase in reactivity for both types of cement, as detected by calorimetry, took place mainly from 20 to 40ºC. The traces at 40 and 60ºC being closer for the PC and almost identical for the BC.

Two additional observations can be highlighted. Firstly, PC and BC display nearly identical mechanical strength performances at 2 days and 60ºC, see Fig. 1. However, PC developed 311.1 J/g, meanwhile, BC released 189.4 J/g (or 39% less heat). This behavior reflects the lower hydration heat of belite and its activated reactivity at mild temperatures. Secondly, the hydration heats at 2 days of BC at 40 and 60ºC are very similar, 187.9 and 189.4 J/g, respectively. However, the mechanical strengths (both compressive and flexural) are much higher at 60ºC, see Fig. 1 panels (b) and (e). This behavior is not captured by the cumulative heat, due to the low hydration heat of belite, but evidenced in the Rietveld quantitative study as the belite hydration degree at 2 days and at 40 and 60ºC are 13 and 34%, respectively, see Table 2. These results emphasize the importance of a multi technique approach.

Finally, it is noted that the calorimetric characterization, as well as thermal analysis and powder diffraction, is carried out for pastes but they are related to the mechanical strength developments of mortars. Therefore, calorimetric measurements were also carried out at 40 and 60ºC for the mortars to determine if the sand significantly modifies the paste hydration kinetics, see Fig. 4. On the one hand and as previously reported [41], the kinetics at early ages are slightly enhanced for mortars, before the main heat flow peak, very likely due to the different shearing conditions when mechanically dispersing the suspensions. On the other hand, the overall heat developed at 7 days is

always slightly smaller for the mortars than for the corresponding pastes. This was also expected as the nominal w/c ratio of pastes and mortars were identical but the sand adsorbs a small amount of water and hence, the effective w/c ratio in mortars, i.e. available for cement hydration, is slightly lower. In any case, the reported results show that the sand does not importantly modify the T-dependent behavior previously discussed for the PC and BC pastes.

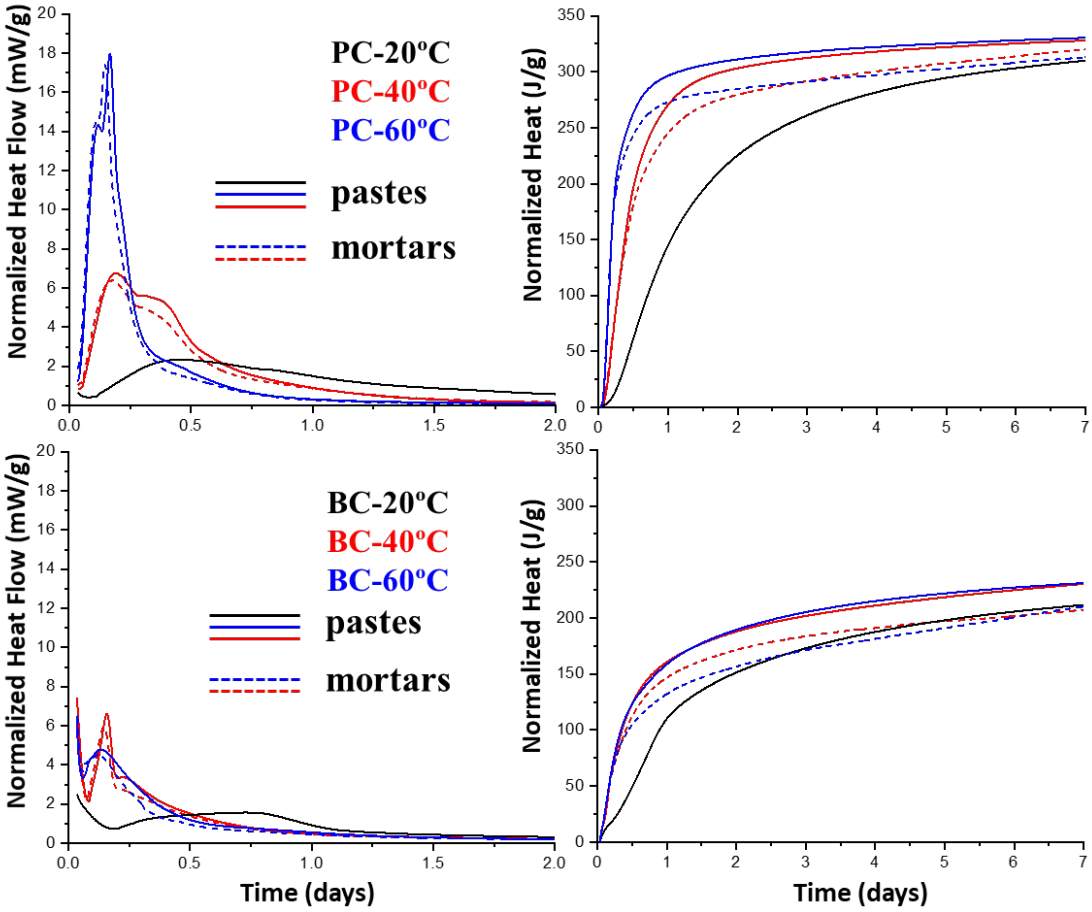

Fig. 4. Calorimetric study as a function of temperature for Portland cement (top) and belite cement (bottom) binders. Heat flow development (curves shown up to 2 days for better visualization) for PC (a) and BC (c). Cumulative heat up to 7 days for PC (b) and BC (d). Continuous and dashed traces for pastes and mortars, respectively.

3.6. ^{29}Si MAS-NMR study. The BC and PC pastes hydrated at 28 days and at 20ºC and 60ºC were also studied by ^{29}Si MAS-NMR. Fig. 5 shows the spectra and their deconvolutions in single components. The signals observed at approximately -79 and -85 ppm are attributed to the Q^1 and Q^2 Si units, respectively. Moreover, the presence of the band situated around -82 ppm is assigned to Q^2 (1Al) [42,43]. Q^1 is associated with silicate end chain units and Q^2 indicates the presence of silicate in intermediate chain positions. Therefore, larger Q^2 relative intensities directly mean larger average silicate chains. Additionally, Q^2(1Al) units represent mid-chain groups in which one of the adjacent tetrahedra contained aluminum. Depending on the case, the silicate mean chain length (MCL) can be determined from the expression, $MCL=2(Q^1+Q^2)/Q^1$ or $MCL=2(Q^1+Q^2+(3/2)Q^2(1Al))/Q^1$ [42]. The MCL values for the PC and BC pastes cured at 20ºC are quite close, 3.05 and 2.96, respectively. At 60ºC, these values increase up to 4.22 and 4.62 for PC and BC, respectively. This shows that the degree of the silicate polymerization in the C-S-H gel increases at high temperatures which is in agreement with previous publications for PC [44,45]. Table S3 gives the areas for the bands that were used to determine the MCL values just reported. Finally, and in agreement with the RQPA study shown above, the reaction degree of the calcium silicate phases increased with the curing temperature as the Q^0 band intensities were lower at higher temperatures. This behavior is more pronounced for belite in BC pastes.

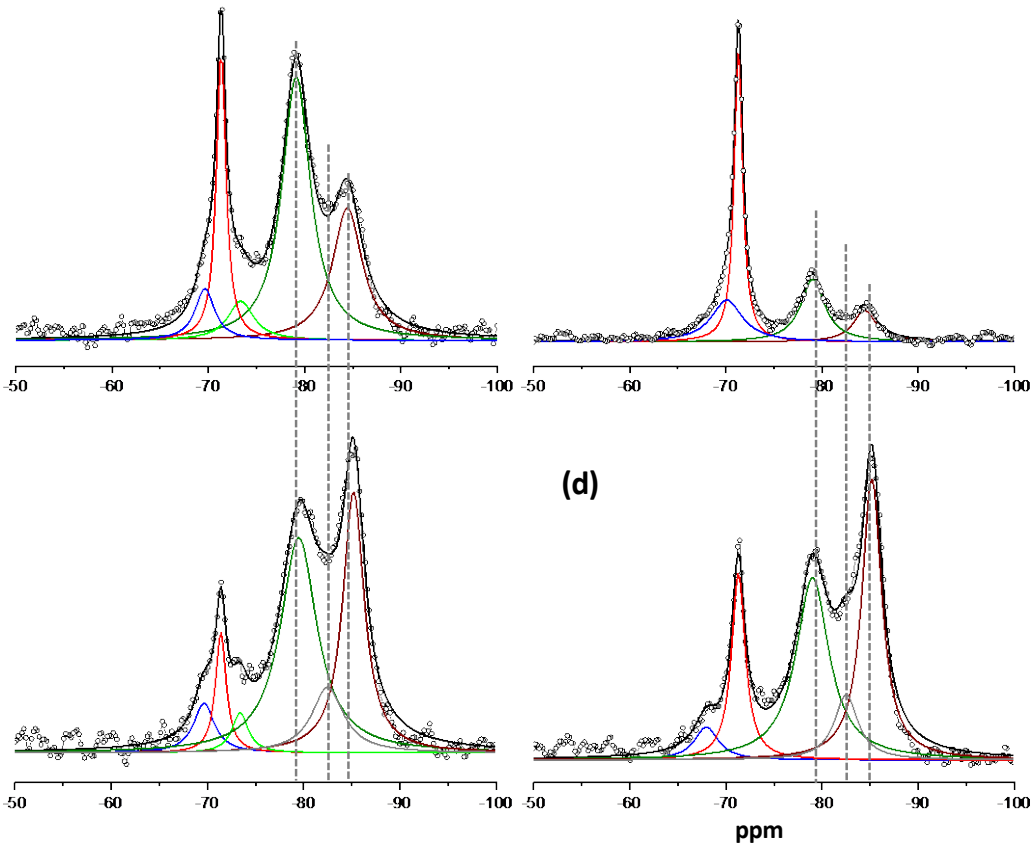

Fig. 5. ^{29}Si MAS-NMR spectra showing the deconvolution of the signals for pastes hydrated during 28 days: (a) PC at 20ºC, (b) BC at 20ºC, (c) PC at 60ºC, and (d) BC at 60ºC.

3.7. Mercury intrusion porosimetry study. The pore size distributions and cumulative porosities of cement pastes cured at selected temperatures for 28 days are shown in Fig. 6. As mercury only intrudes the connected porosity, MIP data really represent pore entry size distributions. This results in an underestimation of the volume of the biggest pores as only a fraction is accessible through smaller ones, known as ink-bottle effect. This feature makes the direct comparison of MIP data with results from other techniques difficult. In any case, the evolution within a given series and the comparison between series is quite informative.

The critical pore entry radii for PC pastes slightly evolve with temperature (from ~65 to 40 nm). Moreover, the pore size distribution is wider at 60 ºC which could reflect the pore coarsening with increasing hydrating temperature [15]. This is highlighted with arrows in Fig. 6 (a) and (b). The most conspicuous result from this study is the smaller critical pore entry sizes of BC pastes, see Fig. 6 (c), when compared to those of PC. The critical pore entry sizes for BC also slightly narrows from 20 to 40ºC, from ~30 to 20 nm, due to the increased degree of reaction. This result is in agreement with the RQPA and TA observations reported above, see Table 1. At 60ºC, and as expected, the pore size slightly broadens, see Fig. 6(c).

It is worth noting that the overall MIP-measured porosity fraction for PC pastes, see Fig. 6(b), changes very little with temperature. Conversely, the overall porosity for BC pastes very significantly decreases from 20 to 40ºC, which is in full agreement with the enhanced degree of reaction of belite reported in Table 2. Finally, our MIP study did not reproduce the previously reported finding [16] which showed a significantly larger critical pore entry size at 60ºC.

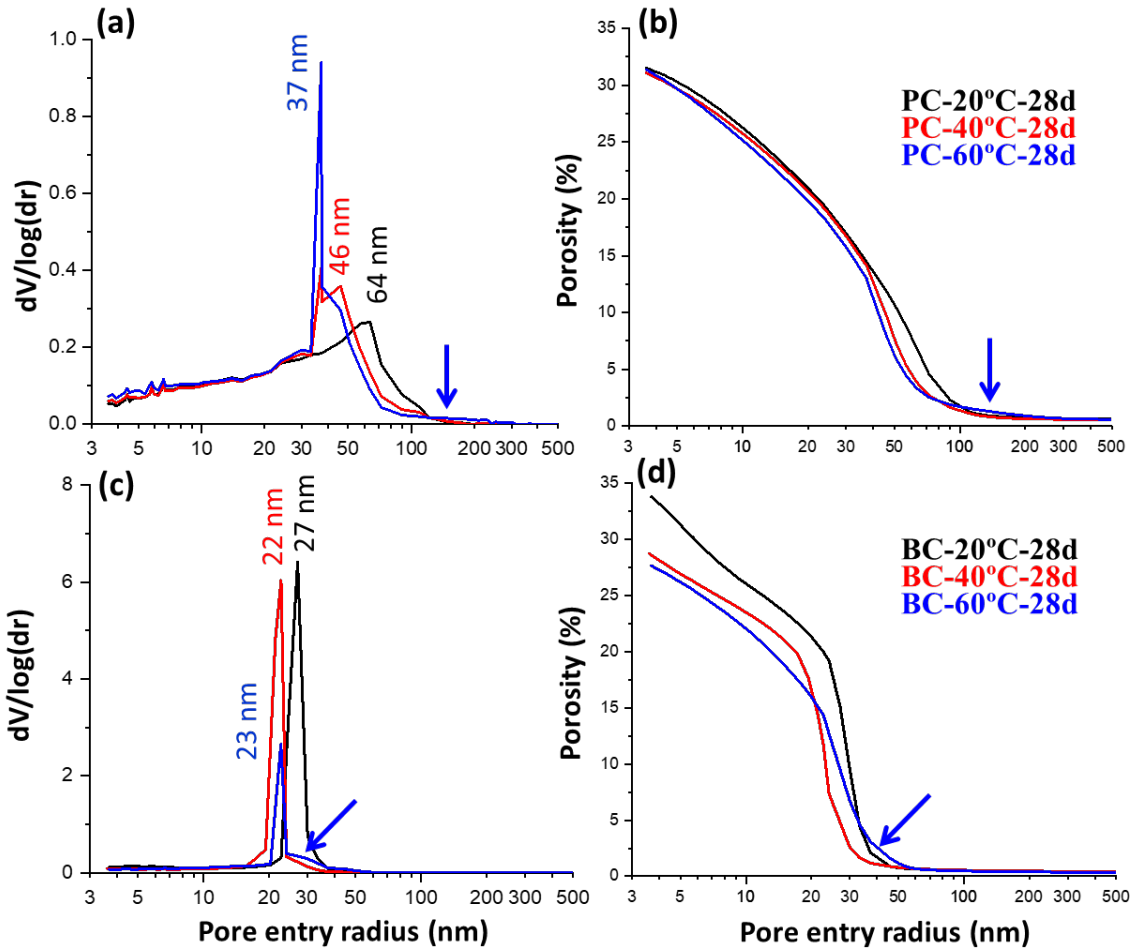

Fig. 6. Textural details, as measured by mercury intrusion porosimetry, for pastes cured at the target temperatures. Differential pore entry size distributions for Portland (a) and belite (c) pastes; and cumulative porosity curves for Portland (b) and belite (d) pastes. The pore coarsening with temperature is highlighted with blue arrows.

3.8. Synchrotron X-ray microtomography analysis. The microstructures of the pastes, without specimen alteration due to sample preparation, have also been studied by synchrotron X-ray microtomography. We benefit from the coherence properties of the synchrotron X-rays by placing the detector 5.5 mm far from the sample which resulted in the edge enhancement also known as X-ray phase-contrast [27] but without several fringes that it could jeopardize the quantitative analysis. From a single propagation-based tomographic data acquisition, two data sets were reconstructed: (i) without Paganin algorithm applied (hereafter, absorption data) and (ii) with Paganin algorithm applied (hereafter, Paganin data) [27]. Fig. 7 displays selected tomographic slices showing glass capillary cross sections (Paganin data) for the PC pastes hydrated at 20, 40 and 60ºC for 28 days. For the sake of comparison, the same tomographic slice (absorption data) for PC hydrated at 20ºC is also shown. In both reconstructions, the anhydrous cement particles (highly absorbing) are whiter and the porous regions (air and water) are darker, the hydrated phases having intermediate grey values. However, it can also be seen that the image contrast (information) in the reconstructed tomograms with Paganin algorithm applied is larger than that present in the amplitude data sets as the differences in gray values of the different components are wider. Fig. 7 also displays similar tomographic slices for the BC pastes. Tomographic data were also taken with hydration time at 20ºC and they are shown in Supplementary Information. Fig. S14 displays the tomographic slices for PC and BC at 3 and 7 days.

In order to illustrate the high spatial resolution nature of the acquired data, Fig. 8 displays an enlarged view of the highlighted region shown in Fig. 7f. It can be seen that a capillary pore of size close to 2 μm is readily measured. Furthermore, the plot profile shown in Fig. 8 allows to follow the three main

components in the studied pastes in the Paganin tomograms: i) porosity (water and air) with grey values ~10000; ii) hydrated components, ~21000-25000; and unhydrated cement particles, ~38000-43000.

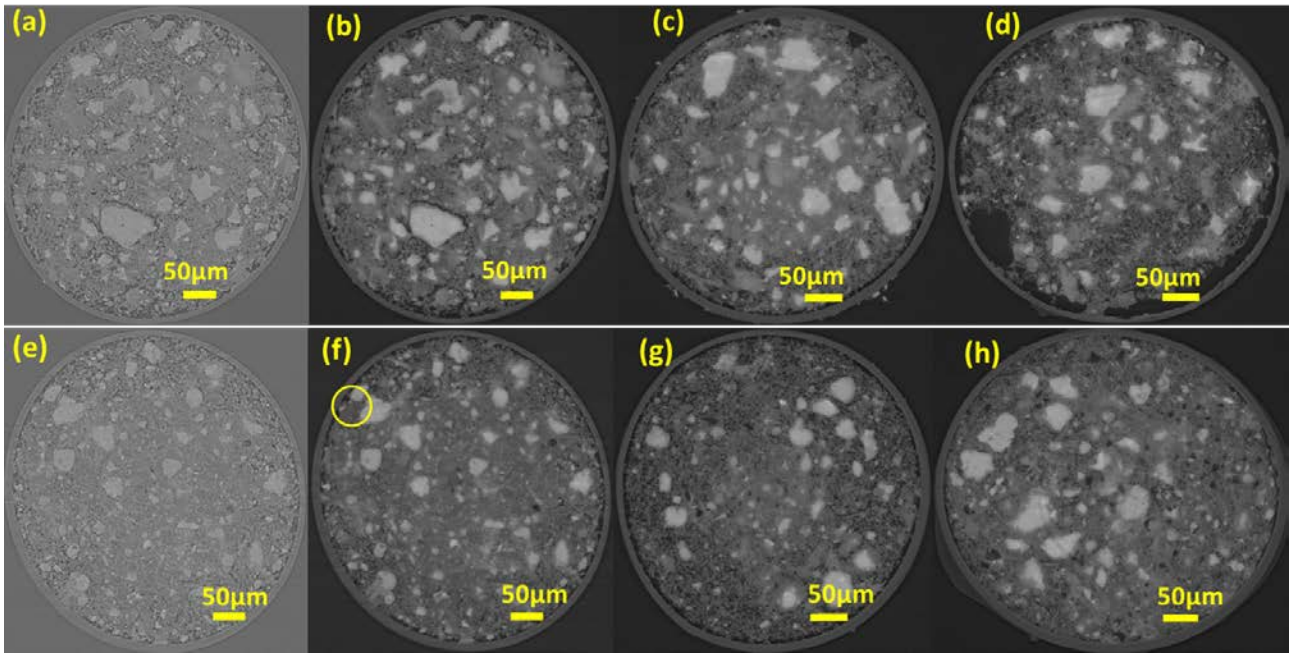

Fig. 7. Reconstructed tomographic slices for the studied pastes as function of temperature (grease sealing). (a) and (e): without Paganin algorithm applied for PC-20ºC-28d#13 and BC-20ºC-28d#50, respectively. (b), (c) and (d): with Paganin algorithm applied for PC-20ºC-28d#13, PC-40ºC-28d#48 and PC-60ºC-28d#45, respectively. (f), (g) and (h) with Paganin algorithm applied for BC-20ºC-28d#50, BC-40ºC-28d#47 and BC-60ºC-28d#44, respectively.

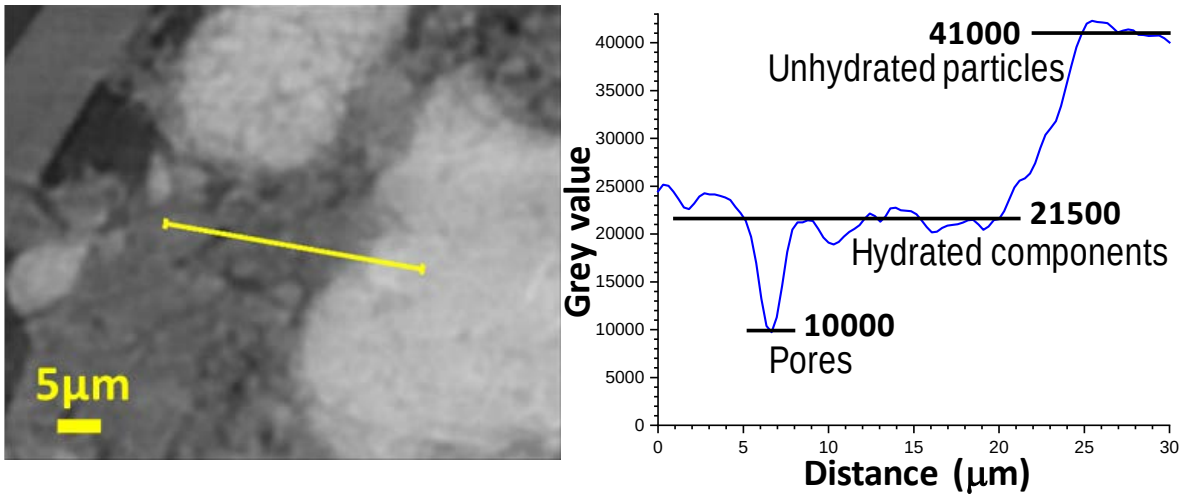

Fig. 8. (Left) Selected (enlarged) view of the Paganin reconstructed tomographic slice for BC-20ºC-28d#50 showing the presence of the main components in the sample. (Right) Plot profile of the grey values along the yellow line depicted in the left panel.

3.8.1. Histogram analysis. A first data analysis can be carried out by inspecting the greyscale histograms (GSHs). For the employed algorithms, the linear attenuation coefficient μ is mapped in the reconstructed tomograms, where the higher is the μ value, the whiter is the corresponding greyscale value. If the chemical stoichiometries and mass densities are known, the μ value can be calculated for the used wavelength [46]. These data are listed in Table 4 and help to understand the observed evolutions in the GSHs. Fig. 9 displays the normalized GSHs (number of voxels corresponding to a given greyscale value divided by the total number of voxels of the analyzed Volume of Interest, VOI) for the pastes cured at 20ºC with increasing hydration time. The VOIs were as large as the mapped cylindrical samples but without incorporating the glass capillaries. As the

images are reconstructed in 16-bits, the GSHs spans from 0 to 65535 integer values. For the absorption tomograms, see Fig. 9b and 9d, it can be seen that the anhydrous component phases are located close to 40000 greyscale values for both types of pastes. The hydrated phases are the main components with greyscale values close to 34000 with a relatively broad distribution reflecting the three main constituents: C-S-H gel, portlandite and ettringite. The water-filled pores cannot be distinguished from the air-filled regions and their greyscale values are similar and lower than ~30000. It is worth noting that as expected, the center of the hydrated components for PC has a larger greyscale value, 34500, than that of the BC pastes, 33300, see Fig. 9b and 9d. This is due to BC pastes containing lower amounts of portlandite, which has the largest attenuation within the hydrated components. Furthermore, hydration kinetics of BCs is slower than that of PCs and this is reflected in the narrowing of the hydrated phase distribution in BC pastes with time, see Fig. 9d. Moreover, the relative amounts of anhydrous components decreased with time as the hydration reaction progressed. Finally, the very narrow band centered as 29500 (in the absorption reconstruction) is due to the large empty volumes (bubbles, cracks from shrinkage, etc.), see Fig. 9b.

Figs. 9 (a) and (c) displays the GSHs for the Paganin data for PC and BC pastes, respectively. The advantages can be clearly seen in these datasets, when compared to the absorption ones, as the separation between the components is much wider. Specifically, the greyscale difference between the anhydrous and hydrated components is larger. Moreover, the porous volumes and void regions now have very low greyscale values close to 10000-12000. This significantly helps in the segmentation stage. It is worth noting that the widths of the hydrated component band for PC pastes did not significantly evolve with hydration time, see Fig. 9 (a), being close to 6500 grey values. Conversely, the hydrated bands for BC pastes sharpened with time, from 8000 to 6000 grey values, see Fig. 9 (c), indicating the important progress of the hydration reactions in this time frame. The sharp bands centered at grey values ~11000, Paganin data, are due to air-filled big pores. This is demonstrated in Fig. S15, for PC-20ºC-28d#13 and BC-60ºC-28d#44 as examples, where the histograms for VOIs including and leaving out the big pore are depicted.

Table 4

Physical data for the main component phases in the studied cement pastes.

Component phase	**Stoichiometry**	**Mass density / g·cm^{-3}**	**μ / cm^{-1}**
Water	H_2O	1.00	1.5
AFt	$Ca_6Al_2(SO_4)_3(OH)_{12}\cdot 26H_2O$	1.78	14.6
AFm	$Ca_4Al_2(OH)_{12}(SO_4)\cdot 6H_2O$	2.02	20.5
C-S-H	$(CaO)_{1.8}(SiO_2)(H_2O)_4$	2.11[#]	23.7
Cc	$CaCO_3$	2.71	34.5
CH	$Ca(OH)_2$	2.23	37.3
C_3A	$Ca_3Al_2O_6$	3.05	46.5
C_2S	Ca_2SiO_4	3.30	52.7
C_3S	Ca_3SiO_5	3.15	54.7
C_4AF	Ca_2AlFeO_5	3.73	89.8

[#] Mass density at the microscale for water saturated nanocrystalline C-S-H gel is taken from [47].

For selecting the greyscale threshold, and in the absence of clear valleys between the contributions, the tangent-slope approach, of the histograms, was used [48]. The grayscale threshold separating the pores from HP was defined as a point, where a change of tangent-slope for both contributions occurred, see Figs 9 and 10 for examples. The derived values are listed in Table 5.

Fig. 10 displays the GSHs for the pastes cured for 28 days at mild temperature for VOI leaving out the big pores. Several observations can be drawn from the inspection of these traces. Firstly, the centers of the hydrated component bands kept approximately constant for PC pastes with temperature

close to 34700 grey value, see Fig. 10(b). Conversely, the position of the centers for BC pastes evolves with temperature from ~33300 to ~34500. We justify this increase in the overall X-ray absorption of BC hydrated components because the decomposition of AFt and mainly the larger fraction of portlandite formed at higher temperature which was observed from RQPA, see results in Table 2. Secondly and importantly, the width of the GSH for the hydrate components in PC markedly increases at 60 ºC, see Fig. 10(a), by about ~40%. This is in line with the reported coarsening of C-S-H gel where the density of C-S-H gel increases likely due to the conversion of gel pore water to capillary water [15–17]. This increase in the heterogeneity of the C-S-H is shown in the 60ºC histogram as a broader distribution. Thirdly and importantly, this behavior is not that markedly shown by the BC pastes with temperature, see Fig. 10(c), where the width increase at 60ºC, is ~20%. This result is in agreement with much lower increase of free water, see Table 2, with temperature for BC pastes. Hence, C-S-H gel coarsening with temperature for BC pastes is significantly less important than for PC ones, which contribute to explain that the mechanical properties of belite mortars cured at higher temperatures are comparatively better than those shown by PC mortars.

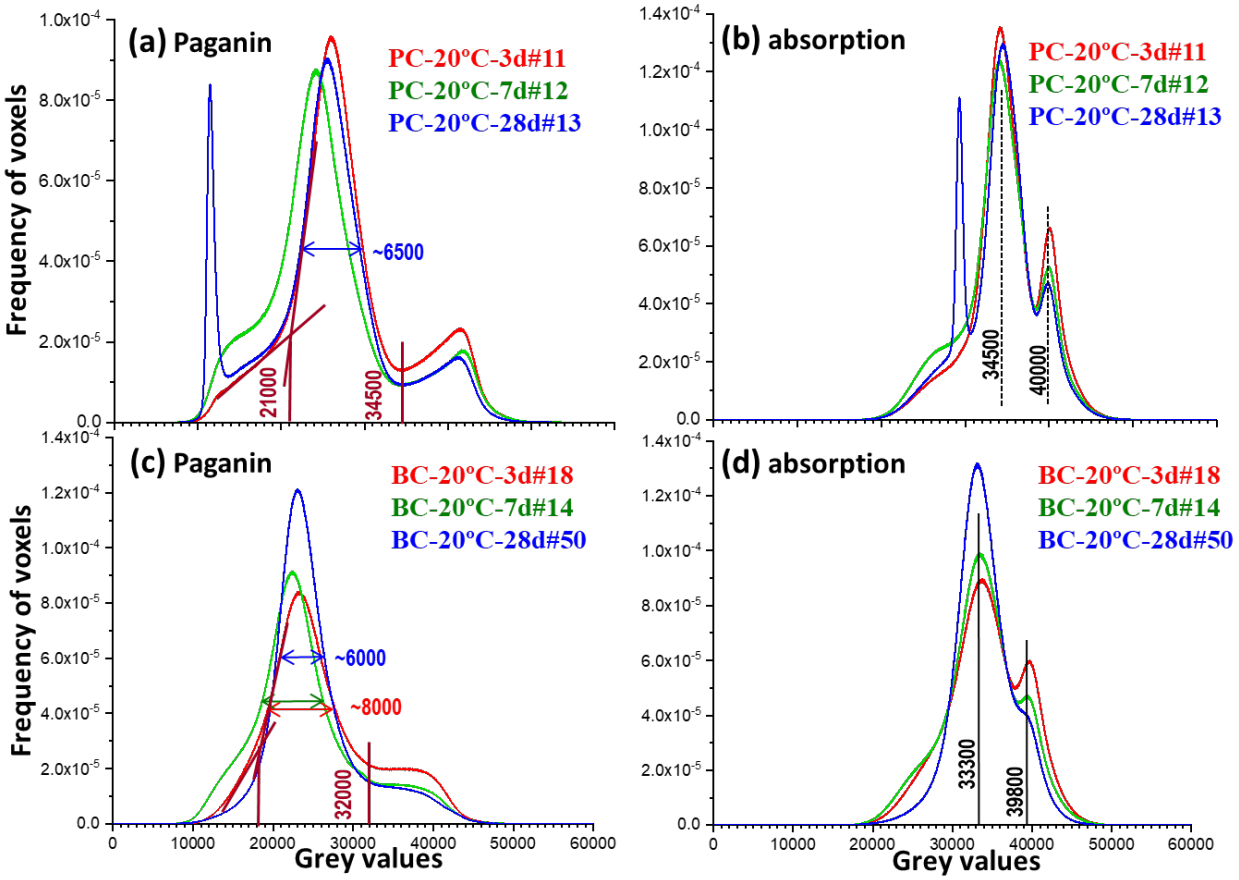

Fig. 9. Volume of interest normalized grayscale histograms. (a) Paganin and (b) absorption traces for PC pastes with hydration time at 20ºC. (c) Paganin and (d) absorption traces for BC pastes with hydration time at 20ºC. Capillaries sealed with grease. The thick brown lines, panels (a) and (c) are the threshold values used for Paganin data segmentation: i) air and water pores have grey values lower than ~20000, ii) hydrated components between ~20000 and ~33000, and iii) unreacted cement phases have grey values larger than ~33000. The tangent-slope approach has been employed for estimating the threshold values between pores and hydrated products.

The comparative temperature behavior is the key output of this study. Therefore, the tomographic results at higher temperatures were repeated in two sets of capillaries independently prepared: one set sealed with grease, see Fig. 10, and the other set sealed by melting the tip of the glass capillaries at high temperatures, see Fig. S16. For this additional set of tomographic studies, the width increase from 20 to 60 ºC for PC pastes was ~45%, see Fig. S16 (a). The analogous study for BC pastes yielded a width increase of ~30%, see Fig. S16 (c). Hence, this different behavior has been firmly established.

Furthermore, reproducibility is always a concern and even more importantly in techniques under development like high-resolution synchrotron X-ray microtomography. Therefore, one repeat for each BC hydrating time paste was also acquired from capillaries filled independently. Fig. S17 displays the comparison of the GHS with good reproducibility for the 7 and 28 days tomograms but less good for the 3 days tomograms.

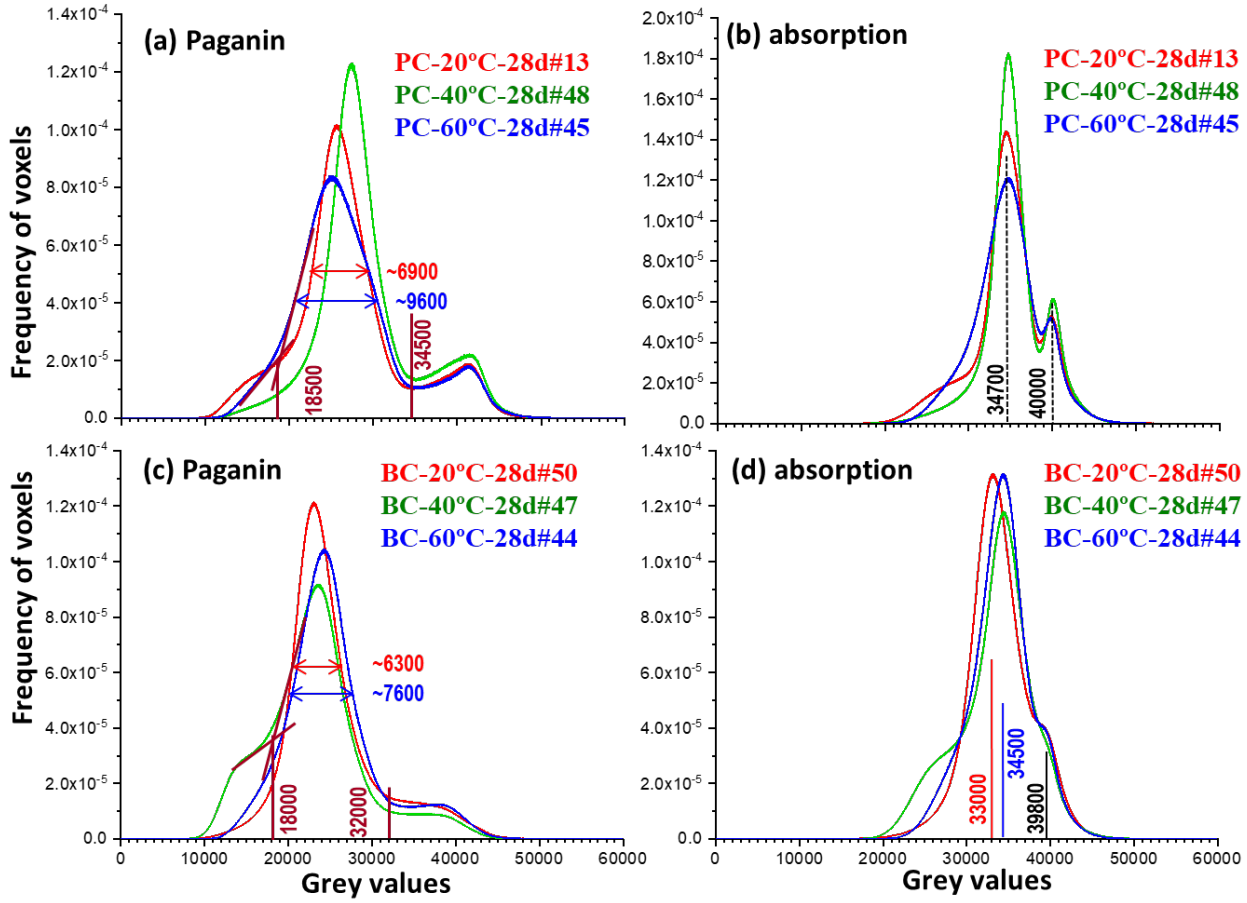

Fig. 10. Volume of interest normalized grayscale histograms with regions with big pores excluded. (a) Paganin and (b) absorption traces for PC pastes with temperature at 28 days of hydration. (c) Paganin and (d) absorption traces for BC pastes with temperature at 28 days of hydration. Capillaries sealed with grease. The thick brown lines, panels (a) and (c) are the threshold values used for Paganin data segmentation as described in Fig. 9. Air and water pores, hydrated phases and unreacted cement phases have grey value ranges as given in Fig. 9 caption.

3.8.2. Segmentation study. All recorded Paganin tomograms were segmented by manual thresholding using Dragonfly software. The thresholds for the component assignment were derived from the GSH shown in Figs. 9 and 10. Specifically, for PC pastes any voxel with a grey value larger than 34500 was labelled as unhydrated cement product (UHP). Voxels with grey values lower than 17000 were labelled as pores. Consequently, the remaining voxels (grey values between 17000 and 34500) were classified as hydrated products (HP). A small amount of calcium carbonate is also accounted within HP component because its X-ray absorption is situated in this range, see Table 4. The corresponding thresholds for BC pastes were similar but not identical: 16500 and 32000, see Figs. 9 and 10. The segmentation results are compiled in Table 5. Fig. 11 displays the rendered volume of the segmented tomograms with temperature. For instance, a big air void/bubble in PC-20ºC-28d#13 is shown, see Fig. 11a which justify the sharp pore band evident in its GSH, see Figs. 9(a) and (b). The rendered segmented volumes of the tomograms for PC and BC with hydration time at 20 ºC are shown in Fig. S18. The selection of the threshold values given above are subjected to errors as there are not deep valleys in the GSHs between the peaks of the three components. Hence, a test was carried out for PC-20ºC-3d#11 where the thresholds were moved by 1000 grey values (i.e.

from 21000 to 20000 for the pore/HP histogram partition and from 34500 to 33500 for the HP/UHP one). The results are given in the footnote of Table 5 and indicate that an error of ~2 vol% comes from the threshold choice.

Several observations can be drawn from the data reported in Table 5 and partly visualized in Fig. 11. Firstly, the porosity changed quite significantly from one capillary to another. This is likely due to problems with the efficient filling of such narrow capillaries. In some cases, large voids with dimensions larger than 100 μm were observed. Furthermore, for some capillaries (but not for all) porosity is concentrated close to the glass capillary walls, see Fig. 11(b). We speculate that this is mainly due to the lack of compaction during the filling of the capillaries with a possible small contribution of chemical shrinking. More research is needed to investigate this behavior by microtomography [49]. As porosity contribution was quite random, Table 5 also reports the segmented values but renormalized just taken into account the hydrated products and the unhydrated cement fraction described as rHP and rUHP, respectively. From the repeats, it can be stated that the reproducibility in the segmented results was relatively poor, 4 vol%. Narrow capillaries, ϕ=0.5 mm, were employed to access to high resolution, as the horizontal field of view was 0.7 mm. It was already known that controlling with w/c ratio and random mineralogical phase distribution in such narrow capillaries was very challenging [50,51]. In general, the segmented amount of unhydrated cement particles, rUHP, ranged 10-20 vol%, being larger than the expected values from RQPA. For instance, the PC paste hydrated at 20ºC for 28 days should have ~9 vol% according to the RQPA and the measured value by microtomography was 14.3 vol%. Conversely, the BC paste hydrated at 20ºC for 28 days should have ~16.5 vol% according to the RQPA and the microtomographic result was 14.9 vol% (the average value of the two segmentations). Overall, there is not a satisfactory agreement between the segmented fractions by tomography and the results by RQPA. Therefore, we conclude that more robust capillary preparation procedure is needed for quantitative component analyses likely implying wider glass tubes to have accurate control of the w/c ratios and reproducible results for component segmentations at high spatial resolution. Our initial intention was to further characterize the temperature evolution of the connectivity of porosity. However, as sample preparation must be improved, it was judged that this type of studies should be carried out after suitable (and reproducible) sample preparations. Furthermore, it must be noted that the computed degree of connectivity of the pore network is very sensitive to the spatial resolution of the tomographic data [50], and hence the best possible spatial resolution should be attained, currently ~1 μm with standard microtomography and ~70 nm with ptychographic nanotomography [47,52]. However, it should also be taken into account that the whole range of pore sizes in the cement binders, down to ~5 nm, cannot be accessed with this level of spatial resolution and the tomographic approach is always an approximation.

Table 5

Segmentation results for the three sets of components (vol%) in the analyzed Paganin tomograms.

Sample	Pores/HP threshold	Pores (vol%)	HP (vol%)	UHP (vol%)	rHP (vol%)	rUHP (vol%)
PC-20ºC-3d#11*	21000	13.3	68.8	17.9	79.4	20.6
PC-20ºC-7d#12	20000	20.1	66.4	13.5	83.1	16.9
PC-20ºC-28d#13	21500	25.0	62.9	12.1	83.9	16.1
BC-20ºC-3d#18	18000	8.3	71.9	19.8	78.4	21.6
BC-20ºC-3d#46	18000	9.9	75.1	15.0	83.4	16.6
BC-20ºC-7d#14	18000	14.9	71.3	13.8	83.8	16.2
BC-20ºC-7d#49	18000	12.2	74.3	13.5	84.6	15.4
BC-20ºC-28d#50	19000	7.0	80.6	12.4	86.7	13.3
BC-20ºC-28d#10	20000	17.1	67.4	15.5	81.3	18.7
PC-40ºC-28d#48	21500	15.5	69.9	14.6	82.7	17.3
PC-40ºC-28d#20	18000	7.8	76.8	15.4	83.3	16.7

PC-60ºC-28d#45	18500	14.5	74.3	11.2	86.9	13.1
PC-60ºC-28d#19	20000	23.1	61.0	15.9	79.3	20.7
BC-40ºC-28d#47	18000	18.7	72.8	8.5	89.5	10.5
BC-40ºC-28d#22	16500	7.4	81.6	11.0	88.1	11.9
BC-60ºC-28d#44	19000	28.0	61.8	10.2	85.8	14.2
BC-60ºC-28d#21	20000	20.5	64.1	15.4	80.6	19.4

* For a segmentation with thresholds 0/20000/33500, the obtained results were 10.8, 70.0 and 19.2 vol% for pores, HP and UHP, respectively.

4. Conclusions

The mechanical strength performances of BC cements increased with curing temperature in the studied range, 20 to 60ºC. This behavior is opposite to that shown by typical PCs where mechanical strengths worsen with increasing curing temperature. The better mechanical performances at mild curing temperature for BC are explained by two findings. The largest contributing factor is the difference in the activation energies of C_2S and C_3S. Rietveld quantitative phases analysis has shown that belite degree of hydration at 28 days in the studied BC increased from 54% to 78%, when raising curing temperature from 20 to 40ºC. This increase in belite reactivity has been backed by thermal analysis (larger portlandite contents), calorimetry (larger heat development) and ^{29}Si MAS-NMR spectrometry (lower Q^0 contribution to the overall spectrum). Furthermore, it is highlighted that at 28 days of hydration of the belite cement, the hydration degrees of alite and belite were nearly identical, (i.e. 87 and 88%, respectively) when cured at 60ºC. Secondly and also playing a role, the curing at mild temperatures for the belite cement did not yield a relevant coarsening of the porosity. This result is derived from the high-resolution synchrotron X-ray microtomographic study and backed by mercury intrusion porosimetry and free water determination. Conversely, the well-known porosity coarsening in PC pastes with temperature is evidenced in the microtomographies.

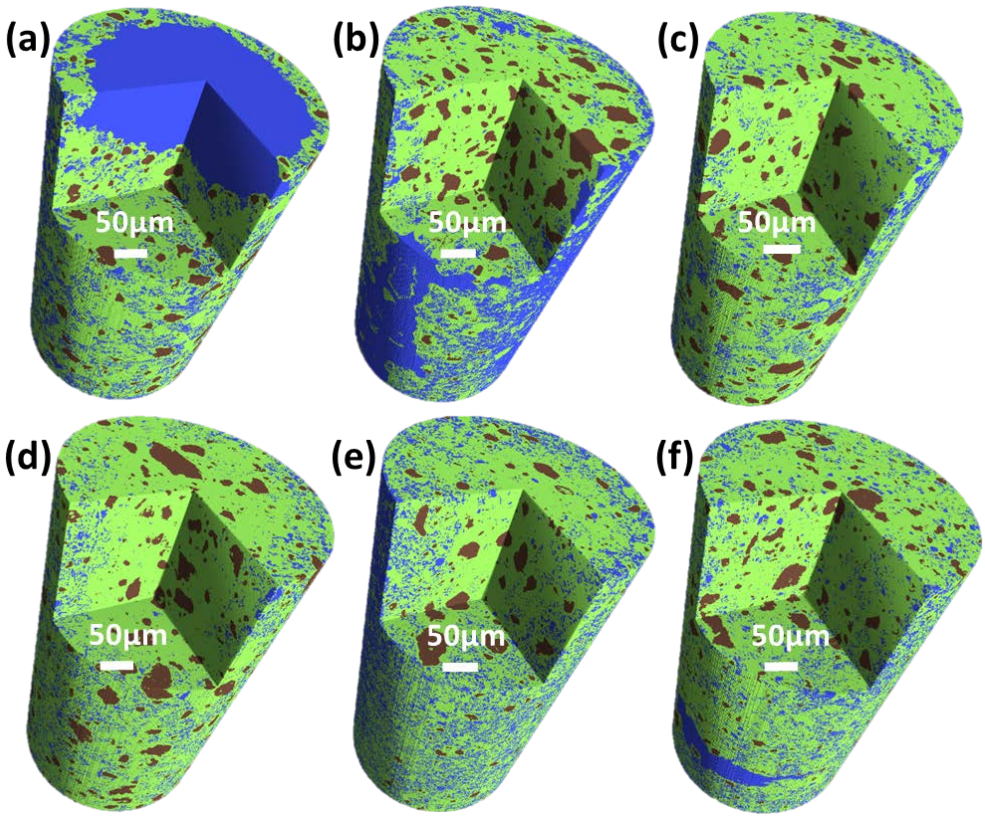

Fig. 11. Rendered volumes displaying the results of the segmentations. Brown represents unhydrated cement components, green represents hydrated products and blue represents porosity (water and air).

(a) PC-20ºC-28d#13, (b) PC-40ºC-28d#48, (c) PC-60ºC-28d#45, (d) BC-20ºC-28d#50, (e) BC-40ºC-28d#47 and (f) BC-60ºC-28d#44. A big (likely air-filled) void in PC-20ºC-28d#13 is shown.

CRediT authorship contribution statement. S Shirani: investigation, methodology, data curation, review & editing; A Cuesta: investigation, methodology, review & editing; A Morales-Cantero: investigation, methodology, review & editing; AG De la Torre: investigation, funding acquisition, review & editing; MP Olbinado: investigation, review & editing; MAG Aranda: conceptualization, supervision, writing original draft, reviewing and editing.

Acknowledgement. Financial support from research grants, BIA2017-82391-R from the Spanish government, which is co-funded by FEDER, and P18-RT-720 from the Andalusian regional government, are gratefully acknowledged. SLS is thanked for granting beamtime at TOMCAT beamline.

Data availability. The synchrotron tomography raw data corresponding to this work are available from the authors upon request. In addition, LXRPD, Thermal analysis, MIP, calorimetry, PSD, ^{29}Si MAS-NMR raw data can be freely accessed on Zenodo at https://doi.org/10.5281/zenodo.4117998, and used under the Creative Commons Attribution license. More details are given in Supplementary Information including the sizes of the tomograms as data transfer could be an issue.

References

[1] UN Environment, K.L. Scrivener, V.M. John, E. Gartner, Eco-efficient cements: Potential, economically viable solutions for a low-CO2, cement-based materials industry, Cem. Concr. Res. 114 (2018) 2–26. https://doi.org/10.1016/j.cemconres.2018.03.015.

[2] H.F.W. Taylor, Cement chemistry, 2nd ed., Thomas Telford Pub, London, UK, 1997.

[3] W.B.C. for Sustainable Development, Cement Sustainability Initiative. Cement Industry Energy and CO2 Performance “Getting the Numbers Right,” Cem. Sustain. Initiat. (2009).

[4] L. Barcelo, J. Kline, G. Walenta, E. Gartner, Cement and carbon emissions, Mater. Struct. 47 (2014) 1055–1065. https://doi.org/10.1617/s11527-013-0114-5.

[5] S.A. Miller, F.C. Moore, Climate and health damages from global concrete production, Nat. Clim. Chang. 10 (2020) 439–443. https://doi.org/10.1038/s41558-020-0733-0.

[6] P.J.M. Monteiro, S.A. Miller, A. Horvath, Towards sustainable concrete, Nat. Mater. 2017 167. 16 (2017) 698–699.

[7] S.J. Davis, N.S. Lewis, M. Shaner, S. Aggarwal, D. Arent, I.L. Azevedo, S.M. Benson, T. Bradley, J. Brouwer, Y.M. Chiang, C.T.M. Clack, A. Cohen, S. Doig, J. Edmonds, P. Fennell, C.B. Field, B. Hannegan, B.M. Hodge, M.I. Hoffert, E. Ingersoll, P. Jaramillo, K.S. Lackner, K.J. Mach, M. Mastrandrea, J. Ogden, P.F. Peterson, D.L. Sanchez, D. Sperling, J. Stagner, J.E. Trancik, C.J. Yang, K. Caldeira, Net-zero emissions energy systems, Science (80-.). 360 (2018). https://doi.org/10.1126/science.aas9793.

[8] K. Van Vliet, R. Pellenq, M.J. Buehler, J.C. Grossman, H. Jennings, F.-J. Ulm, S. Yip, Set in stone? A perspective on the concrete sustainability challenge, MRS Bull. 37 (2012) 395–402. https://doi.org/10.1557/mrs.2012.55.

[9] A.K. Chatterjee, High belite cements—Present status and future technological options: Part I, Cem. Concr. Res. 26 (1996) 1213–1225. https://doi.org/10.1016/0008-8846(96)00099-3.

[10] S.A. Miller, R.J. Myers, Environmental Impacts of Alternative Cement Binders, Environ. Sci. Technol. 54 (2020) 677–686. https://doi.org/10.1021/acs.est.9b05550.

[11] A. Cuesta, A. Ayuela, M.A.G. Aranda, Belite cements and their activation, Cem. Concr. Res. 140 (2021) 106319. https://doi.org/10.1016/j.cemconres.2020.106319.

[12] T. Sui, L. Fang, Z. Wen, J. Wang, Properties of Belite-Rich Portland Cement and Concrete in China, J. Civ. Eng. Archit. 9 (2015) 384–392. https://doi.org/10.17265/1934-7359/2015.04.002.

[13] T. Sui, L. Fan, Z. Wen, J. Wang, Z. Zhang, Study on the Properties of High Strength

Concrete using High Belite Cement, J. Adv. Concr. Technol. 2 (2004) 201–206. https://doi.org/10.3151/jact.2.201.

[14] G.J. Verbeck, Structures and physical properties of cement pastes, in: Proc. 5th Int. Symp. Chem. Cem., 1968: pp. 1–32.

[15] E. Gallucci, X. Zhang, K.L. Scrivener, Effect of temperature on the microstructure of calcium silicate hydrate (C-S-H), Cem. Concr. Res. 53 (2013) 185–195. https://doi.org/10.1016/J.CEMCONRES.2013.06.008.

[16] S. Bahafid, S. Ghabezloo, M. Duc, P. Faure, J. Sulem, Effect of the hydration temperature on the microstructure of Class G cement: C-S-H composition and density, Cem. Concr. Res. 95 (2017) 270–281. https://doi.org/10.1016/j.cemconres.2017.02.008.

[17] A.M. Gajewicz-Jaromin, P.J. McDonald, A.C.A. Muller, K.L. Scrivener, Influence of curing temperature on cement paste microstructure measured by 1H NMR relaxometry, Cem. Concr. Res. 122 (2019) 147–156. https://doi.org/10.1016/J.CEMCONRES.2019.05.002.

[18] S. Brisard, M. Serdar, P.J.M. Monteiro, Multiscale X-ray tomography of cementitious materials: A review, Cem. Concr. Res. 128 (2020) 105824. https://doi.org/10.1016/J.CEMCONRES.2019.105824.

[19] W. Kong, Y. Wei, S. Wang, J. Chen, Y. Wang, Research progress on cement-based materials by X-ray computed tomography, Int. J. Pavement Res. Technol. 13 (2020) 366–375. https://doi.org/10.1007/s42947-020-0119-8.

[20] A. du Plessis, W.P. Boshoff, A review of X-ray computed tomography of concrete and asphalt construction materials, Constr. Build. Mater. 199 (2019) 637–651. https://doi.org/10.1016/j.conbuildmat.2018.12.049.

[21] F. Canonico, Special binders as an alternative to Portland cement, in: 20th Int. Conf. Build. Mater., Weimar, 2018: pp. 410–422.

[22] A.C. Larson, R.B. Von Dreele, General structure analysis system (GSAS), Los Alamos Natl. Lab. Rep. LAUR. 748 (2004) 86–748.

[23] W.A. Dollase, Correction of intensities of preferred orientation in powder diffractometry: application of the march model, J. Appl. Crystallogr. 19 (1986) 267–272. https://doi.org/10.1107/S0021889886089458.

[24] A.G. De La Torre, S. Bruque, M.A.G. Aranda, Rietveld quantitative amorphous content analysis, J. Appl. Crystallogr. 34 (2001). https://doi.org/10.1107/S0021889801002485.

[25] J.D. Zea-Garcia, A.G. De la Torre, M.A.G. Aranda, I. Santacruz, Processing and characterisation of standard and doped alite-belite-ye ’ elimite ecocement pastes and mortars, Cem. Concr. Res. 127 (2020) 105911. https://doi.org/10.1016/j.cemconres.2019.105911.

[26] K.L. Scrivener, R. Snellings, B. Lothenbach, A Practical Guide to Microstructural Analysis of Cementitious Materials, CRC Press, Boca Raton, FL, 2016.

[27] D. Paganin, S.C. Mayo, T.E. Gureyev, P.R. Miller, S.W. Wilkins, Simultaneous phase and amplitude extraction from a single defocused image of a homogeneous object, J. Microsc. 206 (2002) 33–40. https://doi.org/10.1046/j.1365-2818.2002.01010.x.

[28] F. Marone, M. Stampanoni, Regridding reconstruction algorithm for real-time tomographic imaging, J. Synchrotron Radiat. 19 (2012) 1029–1037. https://doi.org/10.1107/S0909049512032864.

[29] A. Morales-Cantero, A.G. De la Torre, A. Cuesta, E. Fraga-Lopez, S. Shirani, M.A.G. Aranda, Belite hydration at high temperature and pressure by in situ synchrotron powder diffraction, Constr. Build. Mater. 262 (2020) 120825. https://doi.org/10.1016/j.conbuildmat.2020.120825.

[30] C.D. Popescu, M. Muntean, J.H. Sharp, Industrial trial production of low energy belite cement, Cem. Concr. Compos. 25 (2003) 689–693. https://doi.org/10.1016/S0958-9465(02)00097-5.

[31] P.K. Metha, P.J. Monteiro, Concrete: Microstructure, Properties, and Materials, 3rd ed., Mcgraw-Hill Professional, 2005.

765 [32] M.A.G. Aranda, A.G. De la Torre, L. Leon-Reina, Rietveld Quantitative Phase Analysis of
766 OPC Clinkers, Cements and Hydration Products, Rev. Mineral. Geochemistry. 74 (2012)
767 169–209. https://doi.org/10.2138/rmg.2012.74.5.

768 [33] B. Lothenbach, F. Winnefeld, C. Alder, E. Wieland, P. Lunk, Effect of temperature on the
769 pore solution, microstructure and hydration products of Portland cement pastes, Cem. Concr.
770 Res. 37 (2007) 483–491. https://doi.org/10.1016/j.cemconres.2006.11.016.

771 [34] B.Z. Dilnesa, E. Wieland, B. Lothenbach, R. Dähn, K.L. Scrivener, Fe-containing phases in
772 hydrated cements, Cem. Concr. Res. 58 (2014) 45–55.
773 https://doi.org/10.1016/j.cemconres.2013.12.012.

774 [35] A. Cuesta, J.D. Zea-Garcia, D. Londono-Zuluaga, A.G. De la Torre, I. Santacruz, O.
775 Vallcorba, M. Dapiaggi, S.G. Sanfélix, M.A.G. Aranda, Multiscale understanding of
776 tricalcium silicate hydration reactions, Sci. Rep. 8 (2018) 8544.
777 https://doi.org/10.1038/s41598-018-26943-y.

778 [36] J. Wang, I. Baco, V. Morin, G. Walenta, D. Damidot, E. Gartner, Hydration mechanisms of
779 cement based on low CO2 clinkers containing belite, ye'elimite and calcium alumino-ferrite,
780 in: Proceeding "THE 7th Int. Symp. Cem. Concr. （ISCC2010), Jinan, China, 2010.

781 [37] M.A.G. Aranda, A.G. De la Torre, Sulfoaluminate cement, in: F. Pacheco-Torgal, S. Jalali, J.
782 Labrincha (Eds.), Eco-Efficient Concr., 2013: pp. 488–522.
783 https://doi.org/10.1533/9780857098993.4.488.

784 [38] C. Naber, F. Bellmann, T. Sowoidnich, F. Goetz-Neunhoeffer, J. Neubauer, Alite dissolution
785 and C-S-H precipitation rates during hydration, Cem. Concr. Res. 115 (2019) 283–293.
786 https://doi.org/10.1016/j.cemconres.2018.09.001.

787 [39] F. Bellmann, T. Sowoidnich, M. Horgnies, E. Gartner, Basic mechanisms of afwillite seeding
788 for acceleration of tricalcium silicate hydration, Cem. Concr. Res. 132 (2020) 106030.
789 https://doi.org/10.1016/j.cemconres.2020.106030.

790 [40] J. Wolf, D. Jansen, F. Goetz-Neunhoeffer, J. Neubauer, Application of thermodynamic
791 modeling to predict the stable hydrate phase assemblages in ternary CSA-OPC-anhydrite
792 systems and quantitative verification by QXRD, Cem. Concr. Res. 128 (2020) 105956.
793 https://doi.org/10.1016/j.cemconres.2019.105956.

794 [41] E. Berodier, K.L. Scrivener, Understanding the Filler Effect on the Nucleation and Growth of
795 C-S-H, J. Am. Ceram. Soc. 97 (2014) 3764–3773. https://doi.org/10.1111/jace.13177.

796 [42] I.G. Richardson, The nature of C-S-H in hardened cements, Cem. Concr. Res. 29 (1999)
797 1131–1147. https://doi.org/10.1016/S0008-8846(99)00168-4.

798 [43] A. Mendes, W.P. Gates, J.G. Sanjayan, F. Collins, NMR, XRD, IR and synchrotron
799 NEXAFS spectroscopic studies of OPC and OPC/slag cement paste hydrates, 44 (2011)
800 1773–1791. https://doi.org/10.1617/s11527-011-9737-6.

801 [44] I.F.S. del Bosque, S. Martínez-Ramírez, M. Martín-Pastor, M.T. Blanco-Varela, Effect of
802 temperature on C–S–H gel nanostructure in white cement, Mater. Struct. Constr. 47 (2014)
803 1867–1878. https://doi.org/10.1617/s11527-013-0156-8.

804 [45] I.F.S. del Bosque, M. Martín-Pastor, S. Martínez-Ramírez, M.T. Blanco-Varela, Effect of
805 Temperature on C3S and C3S + Nanosilica Hydration and C-S-H Structure, J. Am. Ceram.
806 Soc. 96 (2013) 957–965. https://doi.org/10.1111/jace.12093.

807 [46] B.L. Henke, E.M. Gullikson, J.C. Davis, X-Ray Interactions: Photoabsorption, Scattering,
808 Transmission, and Reflection at E = 50− 30,000 eV, Z = 1−92, At. Data Nucl. Data Tables.
809 54 (1993) 181–342.

810 [47] A. Cuesta, A.G. De la Torre, I. Santacruz, A. Diaz, P. Trtik, M. Holler, B. Lothenbach,
811 M.A.G. Aranda, Quantitative disentanglement of nanocrystalline phases in cement pastes by
812 synchrotron ptychographic X-ray tomography, IUCrJ. 6 (2019) 473–491.
813 https://doi.org/10.1107/S2052252519003774.

814 [48] M. Eik, A. Antonova, J. Puttonen, Phase contrast tomography to study near-field effects of
815 polypropylene fibres on hardened cement paste, Cem. Concr. Compos. 114 (2020) 103800.
816 https://doi.org/10.1016/j.cemconcomp.2020.103800.

[49] M. Wyrzykowski, S. Ghourchian, B. Münch, M. Griffa, A. Kaestner, P. Lura, Cement and Concrete Research Plastic shrinkage of mortars cured with a paraffin-based compound – Bimodal neutron / X-ray tomography study, Cem. Concr. Res. 140 (2021) 106289. https://doi.org/10.1016/j.cemconres.2020.106289.

[50] E. Gallucci, K.L. Scrivener, A. Groso, M. Stampanoni, G. Margaritondo, 3D experimental investigation of the microstructure of cement pastes using synchrotron X-ray microtomography (μCT), Cem. Concr. Res. 37 (2007) 360–368. https://doi.org/10.1016/j.cemconres.2006.10.012.

[51] M. Parisatto, M.C. Dalconi, L. Valentini, G. Artioli, A. Rack, R. Tucoulou, G. Cruciani, G. Ferrari, Examining microstructural evolution of Portland cements by in-situ synchrotron micro-tomography, J. Mater. Sci. 50 (2015) 1805–1817. https://doi.org/10.1007/s10853-014-8743-9.

[52] S. Shirani, A. Cuesta, A.G. De la Torre, A. Diaz, P. Trtik, M. Holler, M.A.G. Aranda, Calcium aluminate cement conversion analysed by ptychographic nanotomography, Cem. Concr. Res. 137 (2020) 106201. https://doi.org/10.1016/j.cemconres.2020.106201.

Supplementary Information for

Influence of curing temperature on belite cement hydration: a comparative study with Portland cement

Shiva Shirani[1], Ana Cuesta[1], Alejandro Morales-Cantero[1], Angeles G. De la Torre[1], Margie Olbinado[2], Miguel A. G. Aranda[1]*

[1]*Departamento de Química Inorgánica, Cristalografía y Mineralogía, Universidad de Málaga, Málaga, 29071, Spain.*

[2]*Paul Scherrer Institut, 5232 Villigen PSI, Switzerland*

** email: g_aranda@uma.es*

This file includes:

→ **Raw data availability and description.**

→ **Calculation examples of the portlandite and C-S-H gel contents.**

→ **#3 supplementary Tables:**

→ **#18 supplementary Figures:**

Figure S9. Thermal analysis traces for PC pastes (non-hydration arrested samples) with w/c=0.50, at 40ºC and at a) 2, b) 7, c) 28 days of hydration.

Figure S10. Thermal analysis traces for PC pastes (non-hydration arrested samples) with w/c=0.50, at 60ºC and at a) 2, b) 7, c) 28 days of hydration.

Figure S11. Thermal analysis traces for BC pastes (non-hydration arrested samples) with w/c=0.50, at 20ºC and at a) 3, b) 7, c) 28 days of hydration.

Figure S12. Thermal analysis traces for BC pastes (non-hydration arrested samples) with w/c=0.50, at 40ºC and at a) 2, b) 7, c) 28 days of hydration.

Figure S13. Thermal analysis traces for BC pastes (non-hydration arrested samples) with w/c=0.50, at 60ºC and at a) 2, b) 7, c) 28 days of hydration.

Figure S14. Paganin reconstructed orthoslices hydrated at 20ºC for (a) PC-3d-20ºC#11, (b) PC-7d-20ºC#12, (c) BC-3d-20ºC#18, and (d) BC-7d-20ºC#14.

Figure S15. Volume of interest normalized grayscale histograms for (a) PC-28d-20ºC#13 and (b) BC-60ºC-28d#44, Paganin reconstructions, including (green traces) and excluding (red traces) the big pores. The insets show selected views to depict the cylindrical VOIs employed for these calculations. It is noted that the red VOIs do not contain the big air-filled pores and therefore their corresponding grayscale histograms do not show the sharp band centered at ~11000 grayscale value.

Figure S16. Volume of interest normalized grayscale histograms. (a) Paganin and (b) absorption traces for PC pastes with temperature at 28 days of hydration. (c) Paganin and (d) absorption traces for BC pastes with temperature at 28 days of hydration. Capillaries sealed by melting the tips. The big pore regions have not been included in the VOIs.

Figure S17. Volume of interest normalized grayscale histograms comparing repeats of different capillaries but filled with the same cement paste. (a) Paganin and (b) absorption traces for BC-20ºC-28d#50 and BC-20ºC-28d#10. (c) Paganin and (d) absorption traces for BC-20ºC-7d#14 and BC-20ºC-7d#49. (e) Paganin and (f) absorption traces for BC-20ºC-3d#18 and BC-20ºC-3d#46.

Figure S18. Rendered volumes displaying the results of the segmentations. Brown represents unhydrated cement components, green represents hydrated products and blue represents porosity (water and air). (a) PC-3d-20ºC-Pag#11, (b) PC-7d-20ºC-Pag#12, (c) BC-3d-20-ºC-Pag#18 and (d) BC-7d-20ºC-Pag#14.

• Raw data availability and description:

Tomographic reconstructed raw data (34 tomograms) are available from the authors upon request. Interested researchers in the synchrotron tomographic reconstructed data should be aware of the size of the files which are given in the following table. A hard drive could be necessary.

File Name	**Zipped File Size* (by 7Zip app.)**	**Additional information**
11_PC-20C-3d (Paganin)	22.0Gb	PC-Hydration Age
11_PC-20C-3d (Absorption)	21.9Gb	
12_PC-20C-7d (Paganin)	21.7Gb	
12_PC-20C-7d (Absorption)	21.6Gb	
13_PC-20C-28d (Paganin)	22Gb	
13_PC-20C-28d (Absorption)	21.9Gb	
18_BC-20C-3d (Paganin)	21.8Gb	BC-Hydration Age
18_BC-20C-3d (Absorption)	21.7Gb	
14_BC-20C-7d (Paganin)	21.9Gb	
14_BC-20C-7d (Absorption)	21.8Gb	
50_BC-20C-28d (Paganin)	22.1Gb	
50_BC-20C-28d (Absorption)	22.0Gb	
48_PC-40C-27d (Paganin)	21.7Gb	PC-Temperature
48_PC-40C-27d (Absorption)	21.6Gb	
45_PC-60C-26d (Paganin)	21.7Gb	
45_PC-60C-26d (Absorption)	21.6Gb	
47_BC-40C-27d (Paganin)	21.8Gb	BC-Temperature
47_BC-40C-27d (Absorption)	21.8Gb	
44_BC-60C-26d (Paganin)	22.0Gb	
44_BC-60C-26d (Absorption)	21.9Gb	
20_PC-40C-27d (Paganin)	21.7Gb	PC-Fire
20_PC-40C-27d (Absorption)	21.6Gb	
19_PC-60C-26d (Paganin)	22.1Gb	
19_PC-60C-26d (Absorption)	21.8Gb	
22_BC-40C-27d (Paganin)	22.2Gb	BC-Fire
22_BC-40C-27d (Absorption)	22.1Gb	
21_BC-60C-26d (Paganin)	22.2Gb	
21_BC-60C-26d (Absorption)	22.1Gb	
46_BC-20C-3d (Paganin)	21.9Gb	BC-repeat
46_BC-20C-3d (Absorption)	21.8Gb	
49_BC-20C-7d (Paganin)	22.0Gb	
49_BC-20C-7d (Absorption)	22.0Gb	
10_BC-20C-28d (Paganin)	21.7Gb	
10_BC-20C-28d (Absorption)	21.7Gb	
Total size of all datasets :	**743.4Gb**	

**Original file size for every single dataset is 27.4GB*

Additionally, the raw data for calorimetry, MIP, LXRPD, NMR and PSD are uploaded on Zenodo in text file or excel format. Besides, the thermal analysis files can be open using the TA Universal Analysis software. Data can be accessed at: https://doi.org/10.5281/zenodo.4117998

• Calculation examples of the portlandite and C-S-H gel contents.

For the PC T=20ºC paste at 28 days of hydration, the following calculations were performed.

As it was detailed in the main manuscript, the following chemical reactions are taking into account:

$Ca_3SiO_5 + 5.2\ H_2O \rightarrow (CaO)_{1.8}SiO_2(H_2O)_{4.0}$ (am.) + $1.2Ca(OH)_2$ (cryst.) (3)

$Ca_2SiO_5 + 4.2\ H_2O \rightarrow (CaO)_{1.8}SiO_2(H_2O)_{4.0}$ (am.) + $0.2Ca(OH)_2$ (cryst.) (4)

$0.84\ Ca_2SiO_4 + 0.5\ Ca_4Al_2Fe_2O_{10} + 5H_2O \rightarrow Ca_3AlFe(SiO_4)_{0.84}(OH)_{8.64}$ (am.) + $0.68Ca(OH)_2$ (cryst.) (5)

$0.84\ Ca_3SiO_5 + 0.5\ Ca_4Al_2Fe_2O_{10} + 5.84H_2O \rightarrow Ca_3AlFe(SiO_4)_{0.84}(OH)_{8.64}$ (am.) + $1.52Ca(OH)_2$ (cryst.) (6)

According to equation (5), 1 g of C_4AF consumes 0.60 g of C_2S and gives 1.76 g of amorphous Al- and Fe- siliceous hydrogarnet and 0.21 g of portlandite.
For PC (20ºC) at 28 days, there is 1.9 g of C_4AF left. As it was 6.4 g of C_4AF at t_0 (in the system which includes the added water, 33.3 wt%), 4.5 g of C_4AF has been consumed.
Only 4.0 g of C_4AF are going to react according to equation (5) as there is only 2.4 g of C_2S that has reacted (5.0 g left of C_2S at 28 days and it was 7.4 g of C_2S at t_0). Consequently, 7.0 g of amorphous Al- and Fe- siliceous hydrogarnet and 0.8 g of Portlandite have been formed.

According to equation (6), 1 g of C_4AF consumes 0.79 g of C_3S and gives 1.76 g of amorphous Al- and Fe- siliceous hydrogarnet and 0.46 g of Portlandite.
0.5 g of C_4AF are going to react according to equation (6) and this consumes 0.4 g of C_3S. Consequently, 0.9 g of amorphous Al- and Fe- siliceous hydrogarnet and 0.2 g of Portlandite have been formed.

According to equation (3), 1 g of C_3S gives 1.02 g of C-S-H and 0.39 g of Portlandite.
For PC (20ºC) at 28 days, there is 4.3 g left of C_3S. As it was 32.1 g of C_3S at t_0 (in the system which includes the added water, 33.3 wt%), 27.8 g of C_3S has been consumed. However, 0.4 g of C_3S has been already consumed for equation (5). Consequently, for 27.4 g of C_3S consumed, 28.0 g of C-S-H and 10.7 g of Portlandite have been formed.

In this example, there is no more C_2S left to apply equation (4).

Theoretically, for the PC T=20ºC paste at 28 days of hydration, 28.0 g of C-S-H gel precipitate and 11.8 of portlandite crystallize.

Moreover, the wt% of C-S-H gel can be calculated from the overall ACn values. For instance, 7.9 g of Al- and Fe- siliceous hydrogarnet has been formed. For this reason, C-S-H (wt%)= ACn (wt%)-[Al- and Fe- siliceous hydrogarnet] (wt%); 49.2-7.9=41.3 wt% C-S-H.

For the other samples, the same strategy has been applied. For the samples hydrated at 40ºC and 60ºC, the decomposition of the AFt has also been taking into account, equation (7):
$Ca_6Al_2(OH)_{12}(SO_4)_3 \cdot 26H_2O \rightarrow Ca_4Al_2(OH)_{12}(SO_4) \cdot 6H_2O + 2CaSO_4 \cdot 2H_2O + 16H_2O$ (7)

In this case; C-S-H wt% = ACn(wt%) - [Al- and Fe- siliceous hydrogarnet](wt%) – AFm amorphous (%wt).

- **Tables**

Table S1. Mineralogical analyses (wt%) from laboratory X-ray powder diffraction using the Rietveld method and internal standard (quartz) for the two used cements.

	C_3S	β-C_2S	C_4AF	C_3A	$C_4A_3\overline{S}$	$C\overline{S}$	$C\overline{S}\cdot0.5H$	$C\overline{S}\cdot2H$	$C\overline{C}$	K_2SO_4	MgO	ACn
PC	48.1(3)[$]	11.0(7)	9.6(4)	2.8(1)	-	-	0.9(1)	0.8(1)	2.8(1)	0.8(1)	-	23.2
BC	24.6(4)[#]	44.2(3)	10.4(4)	1.0(1)	1.9(1)	1.6(1)	-	-	1.3(1)	-	1.4(1)	13.6

[$] The fit was carried out with 100% M3 polymorph.
[#] The fit was carried out with a mixture of M1 and M3 polymorphs. Results: 3.0 wt% of M3 and 21.6wt% of M1.

Table S2. Elemental analyses (wt% expressed as oxide contents) from X-ray fluorescence for the two used cements.

	CaO	SiO_2	SO_3	Al_2O_3	Fe_2O_3	MgO	K_2O	others	LoI
PC	62.9	19.7	3.4	5.0	3.4	1.5	1.1	0.3	2.7
BC	59.3	21.4	4.8	4.3	2.8	2.7	0.9	0.9	2.9

Table S3. Summary of the ^{29}Si MAS-NMR spectrum analyses for the studied samples.

Sample	Q^1 position/ ppm	Q^1 area /%	Q^2 (1Al) position/ ppm	Q^2 (1Al) area /%	Q^2 position/ ppm	Q^2 area /%	MCL
PC-20ºC-28d	-79.1	46.2	-	-	-84.4	24.3	3.05
PC-60ºC-28d	-79.5	42.5	-82.5	11.3	-85.2	30.3	4.22
BC-20ºC-28d	-79.0	25.0	-	-	-84.4	12.0	2.96
PC-60ºC-28d	-79.0	36.5	-82.5	9.3	-85.2	33.9	4.62

- **Figures.**

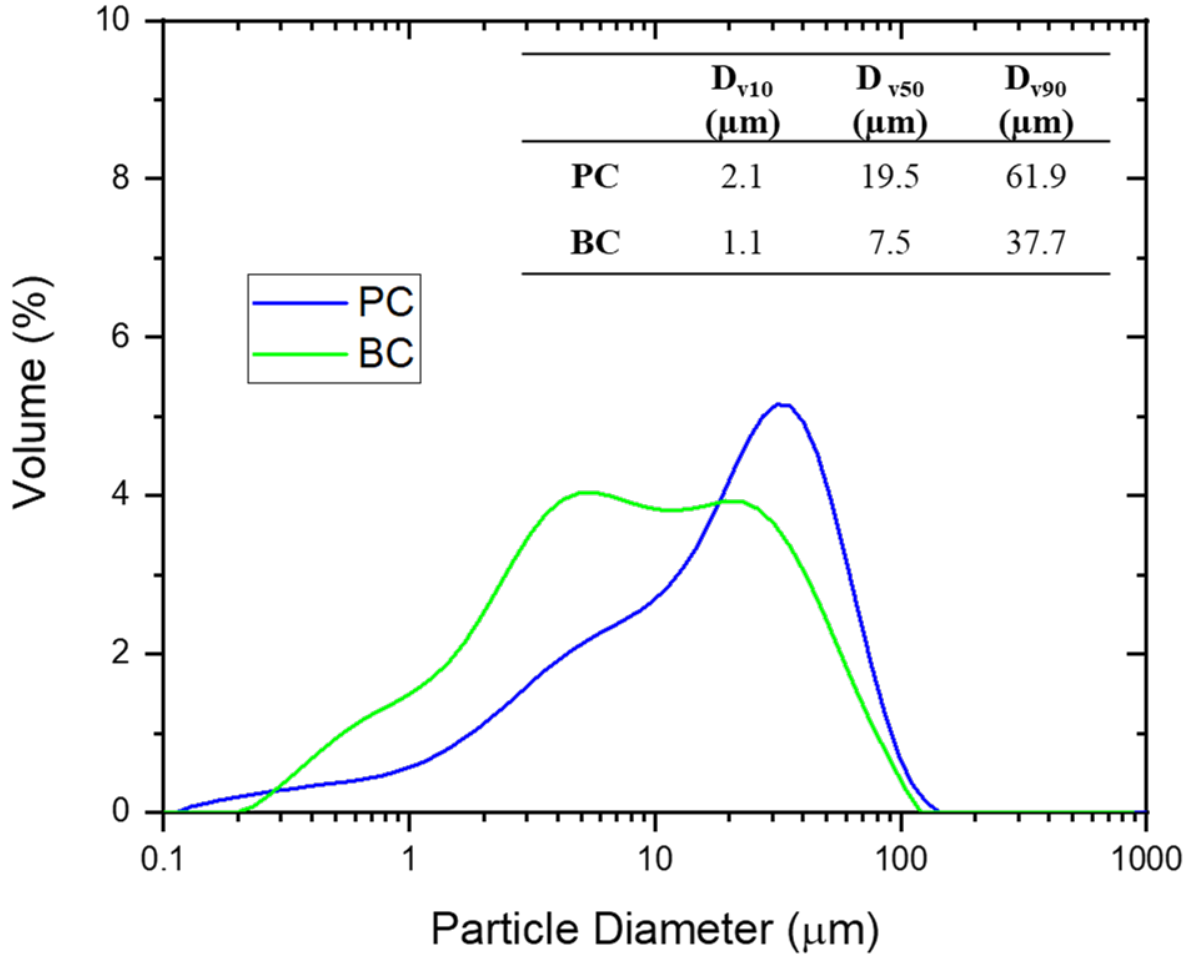

	D_{v10} (μm)	D_{v50} (μm)	D_{v90} (μm)
PC	2.1	19.5	61.9
BC	1.1	7.5	37.7

Figure S1. Particle size distribution plots for the two studied anhydrous samples: Portland cement (blue trace) and belite cement (green trace).

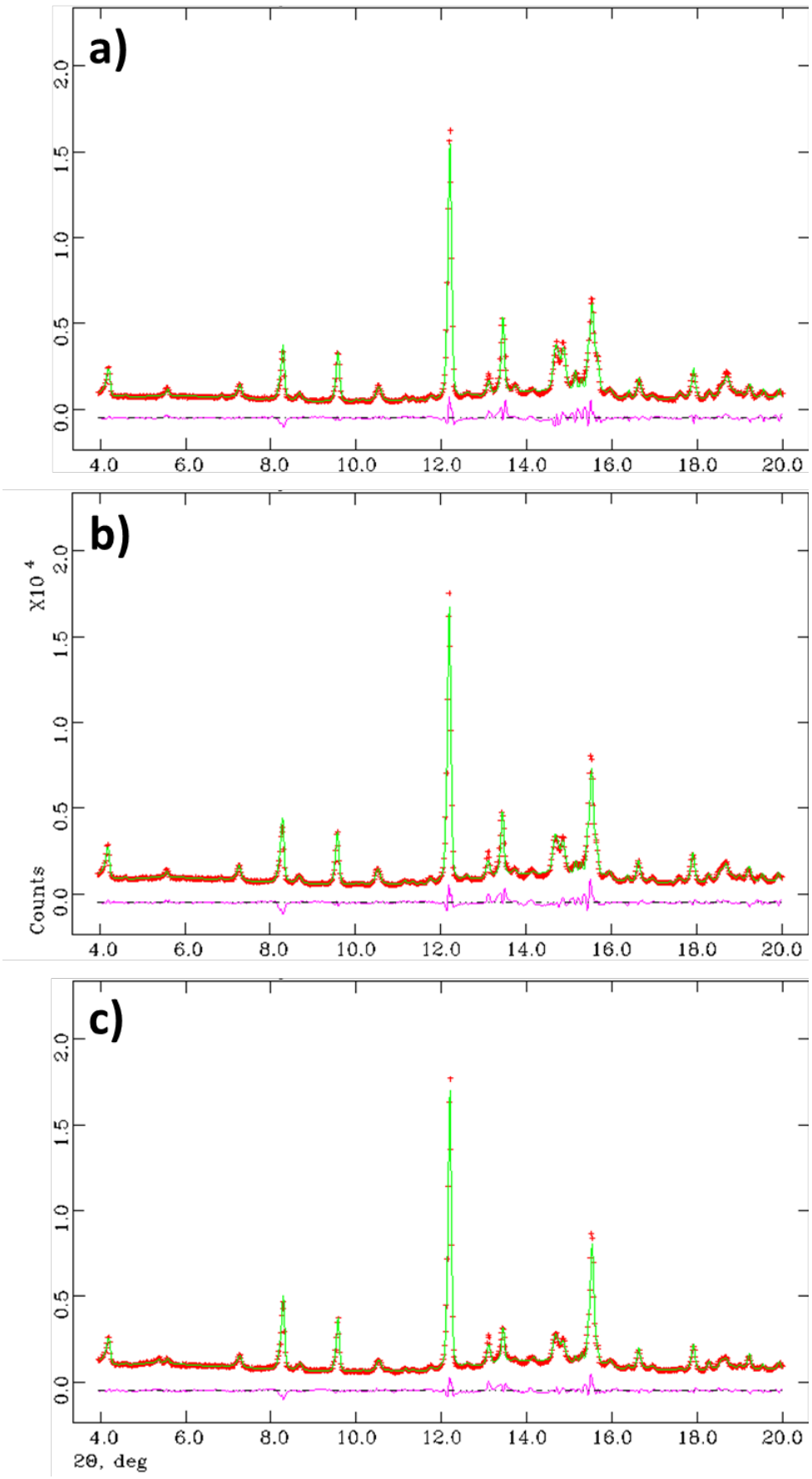

Figure S2. Selected region of the Rietveld plots (Mo-Kα_1 strictly monochromatic radiation, λ=0.71 Å) for PC pastes with w/c=0.50, at 20ºC and at a) 3, b) 7, c) 28 days of hydration.

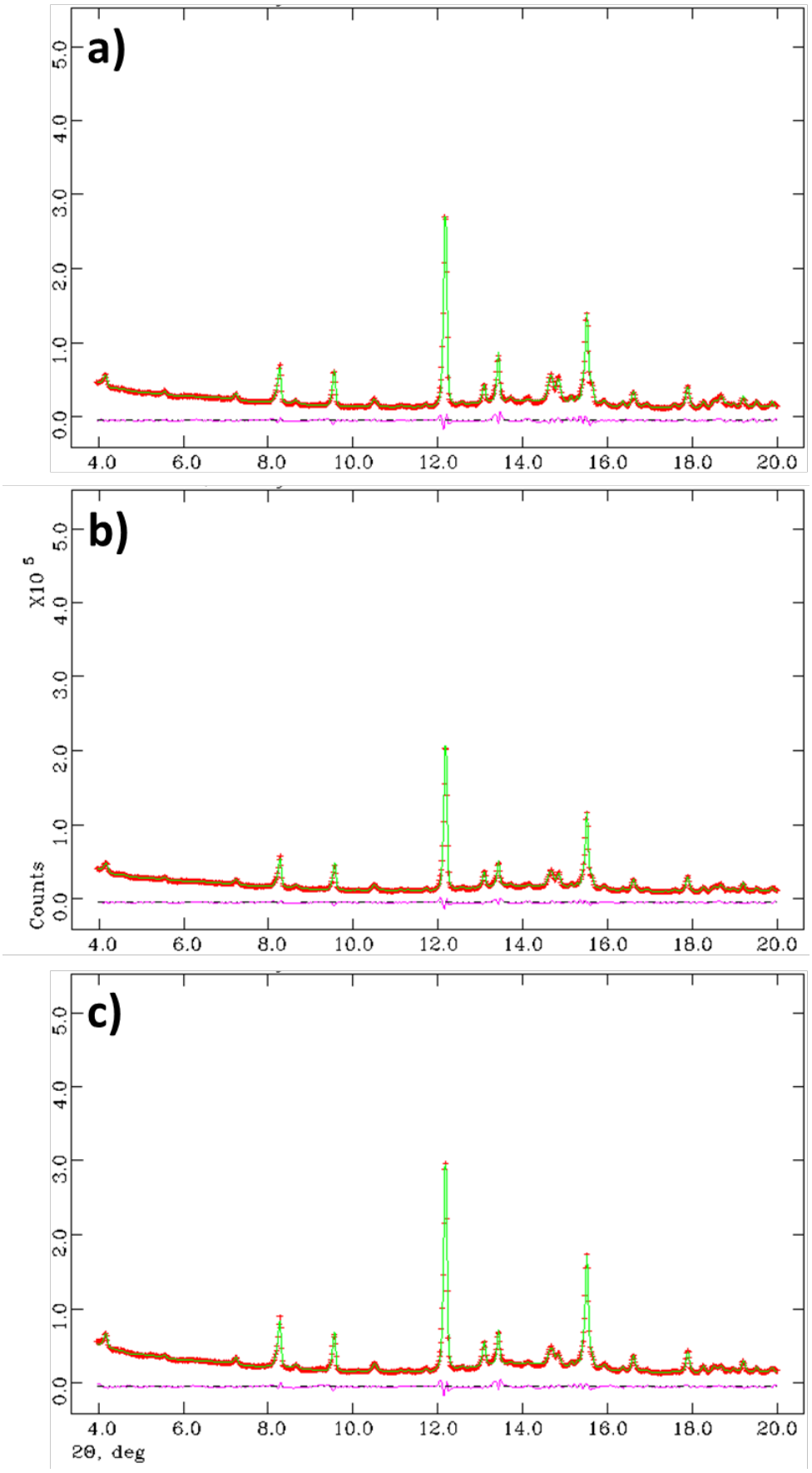

Figure S3. Selected region of the Rietveld plots (Mo-Kα_1 strictly monochromatic radiation, λ=0.71 Å) for PC pastes with w/c=0.50, at 40ºC and at a) 2, b) 7, c) 28 days of hydration.

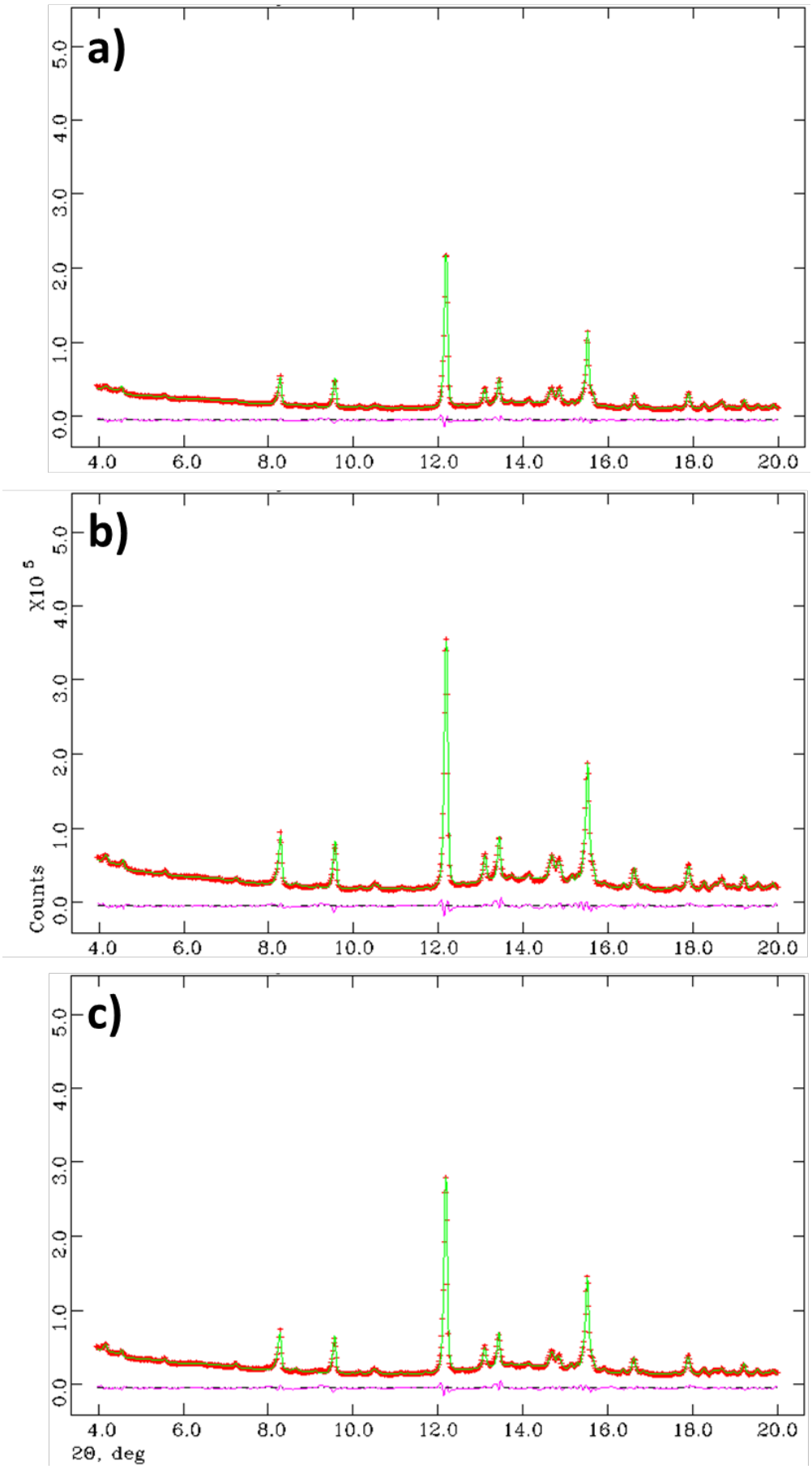

Figure S4. Selected region of the Rietveld plots (Mo-Kα_1 strictly monochromatic radiation, λ=0.71 Å) for PC pastes with w/c=0.50, at 60ºC and at a) 2, b) 7, c) 28 days of hydration.

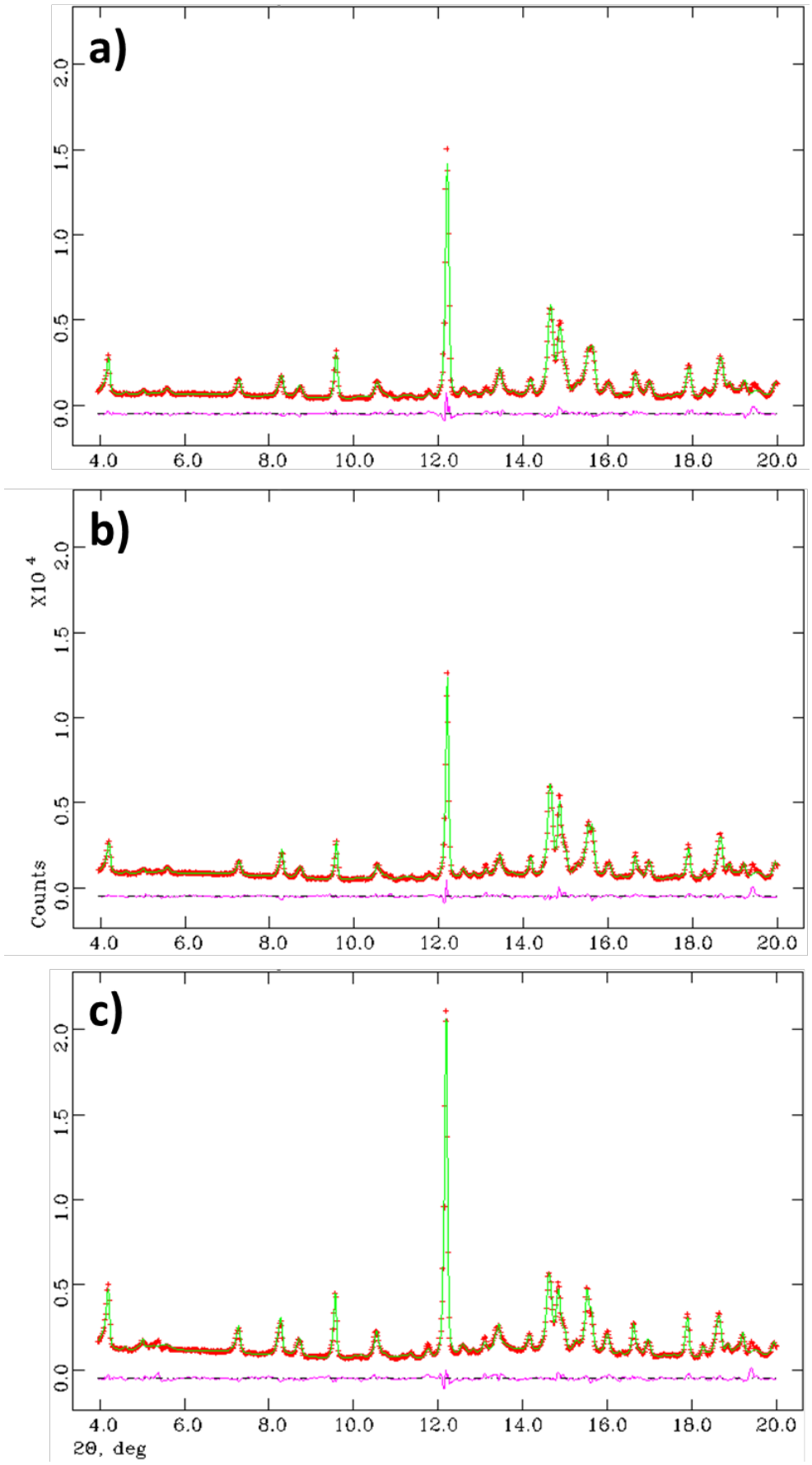

Figure S5. Selected region of the Rietveld plots (Mo-Kα_1 strictly monochromatic radiation, λ=0.71 Å) for BC pastes with w/c=0.50, at 20ºC and at a) 3, b) 7, c) 28 days of hydration.

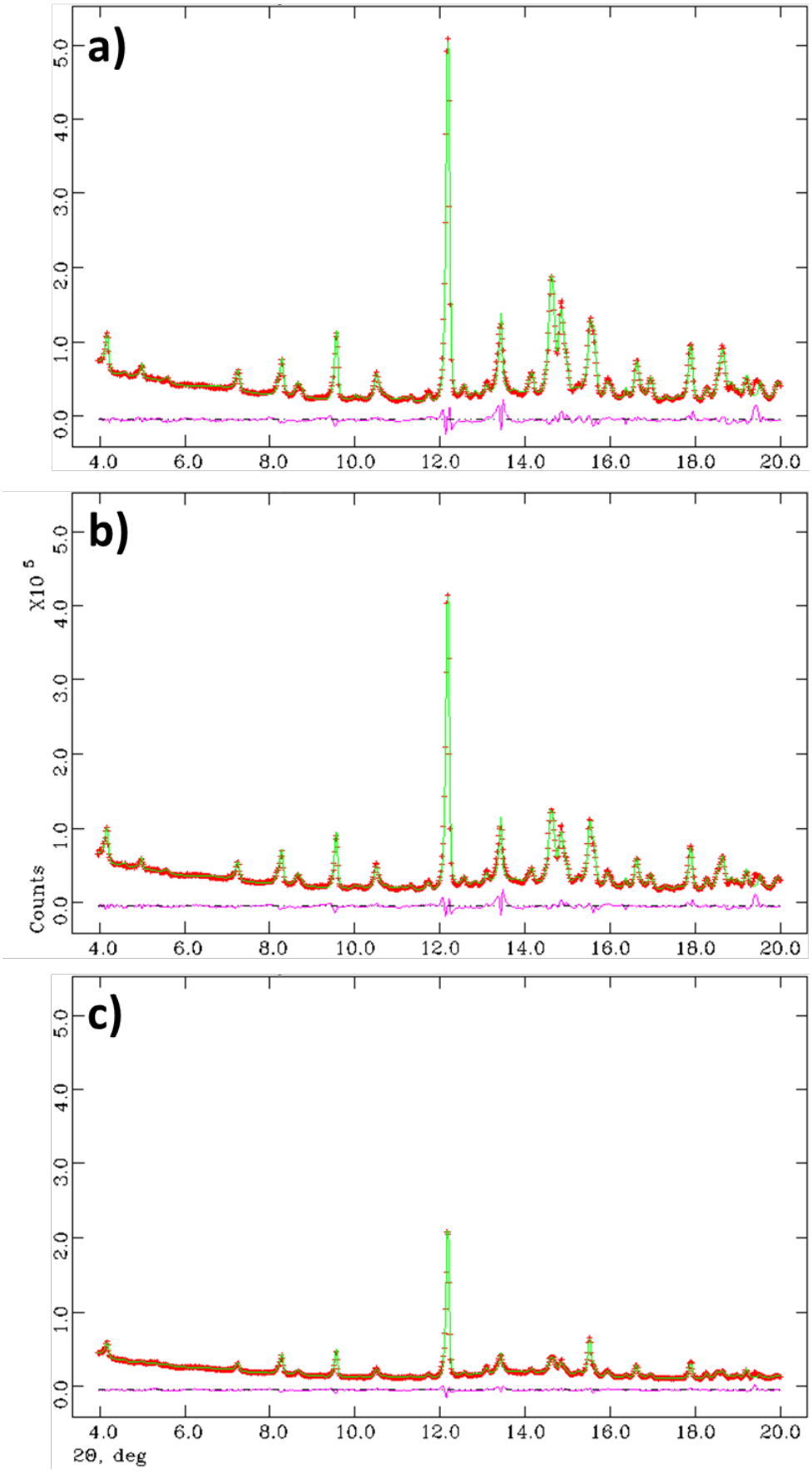

Figure S6. Selected region of the Rietveld plots (Mo-Kα_1 strictly monochromatic radiation, λ=0.71 Å) for BC pastes with w/c=0.50, at 40ºC and at a) 2, b) 7, c) 28 days of hydration.

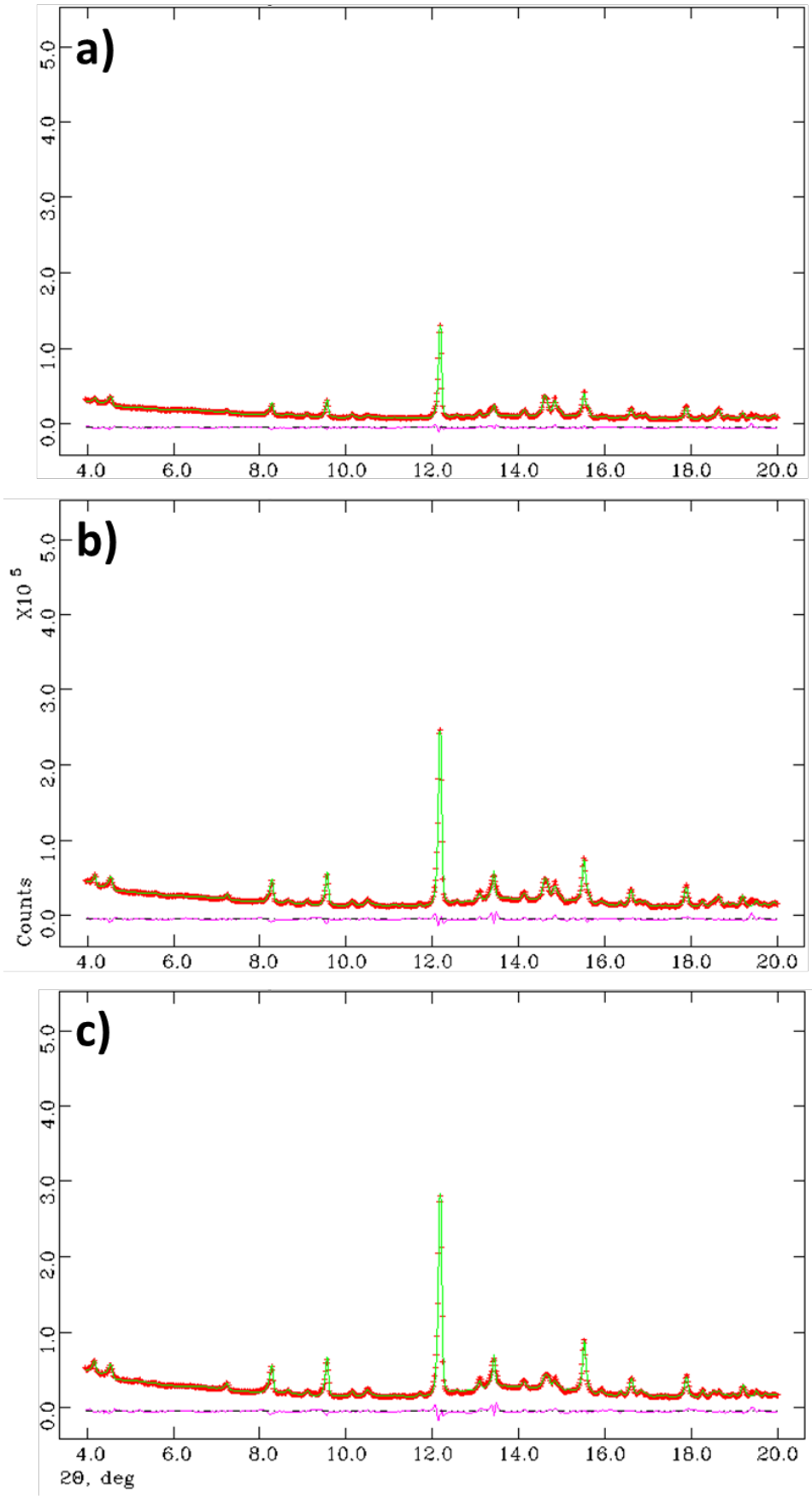

Figure S7. Selected region of the Rietveld plots (Mo-Kα_1 strictly monochromatic radiation, λ=0.71 Å) for BC pastes with w/c=0.50, at 60ºC and at a) 2, b) 7, c) 28 days of hydration.

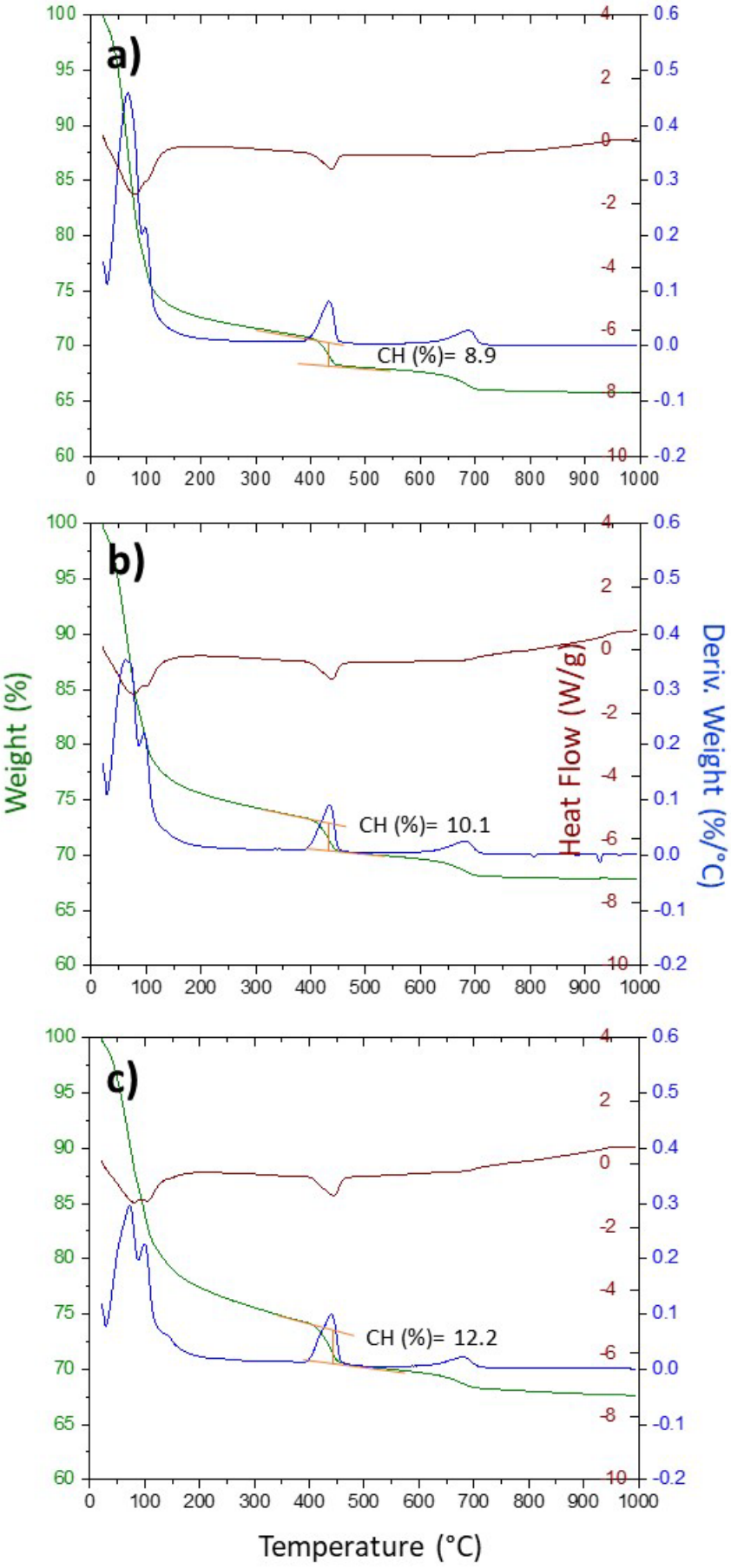

Figure S8. Thermal analysis traces for PC pastes (non-hydration arrested samples) with w/c=0.50, at 20ºC and at a) 3, b) 7, c) 28 days of hydration.

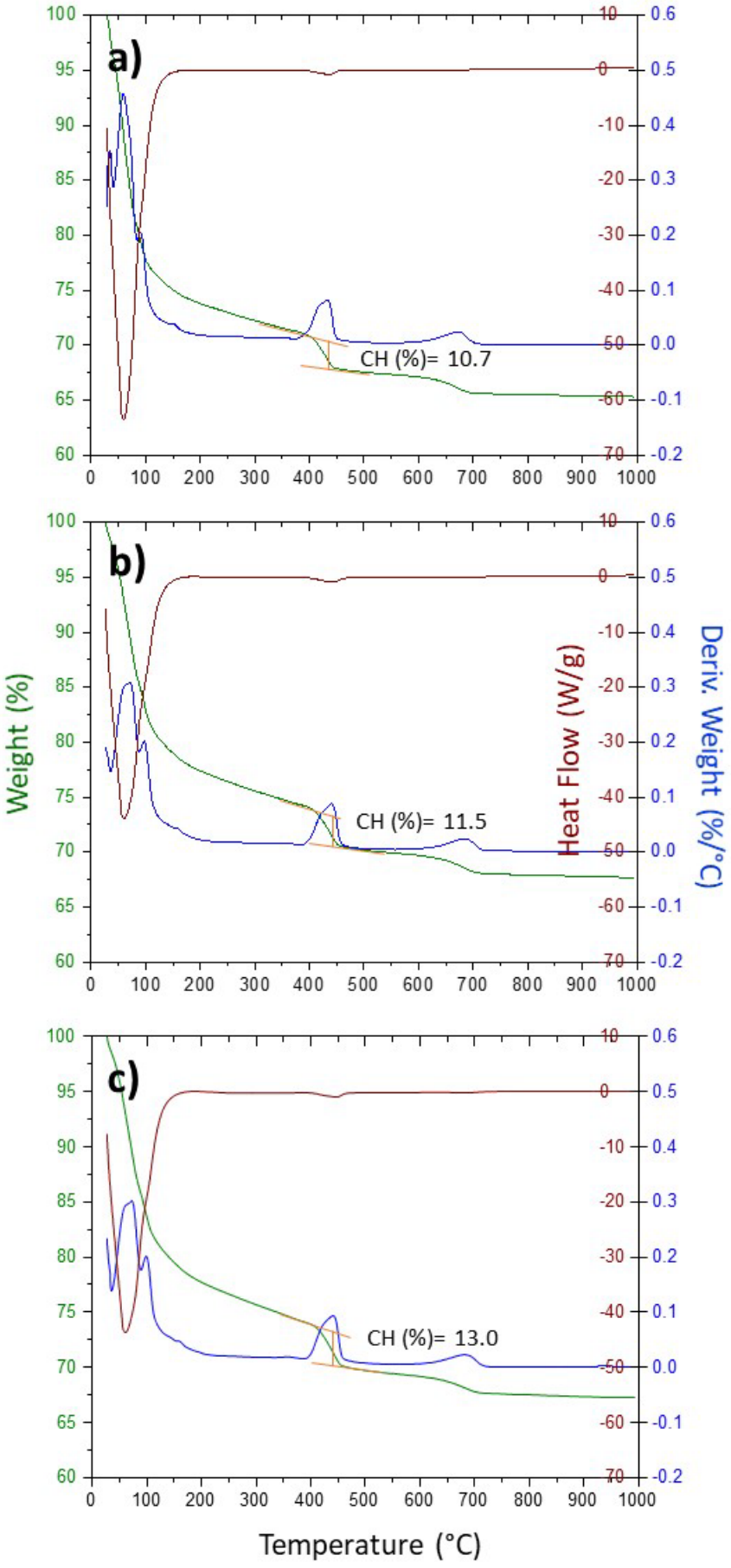

Figure S9. Thermal analysis traces for PC pastes (non-hydration arrested samples) with w/c=0.50, at 40ºC and at a) 2, b) 7, c) 28 days of hydration.

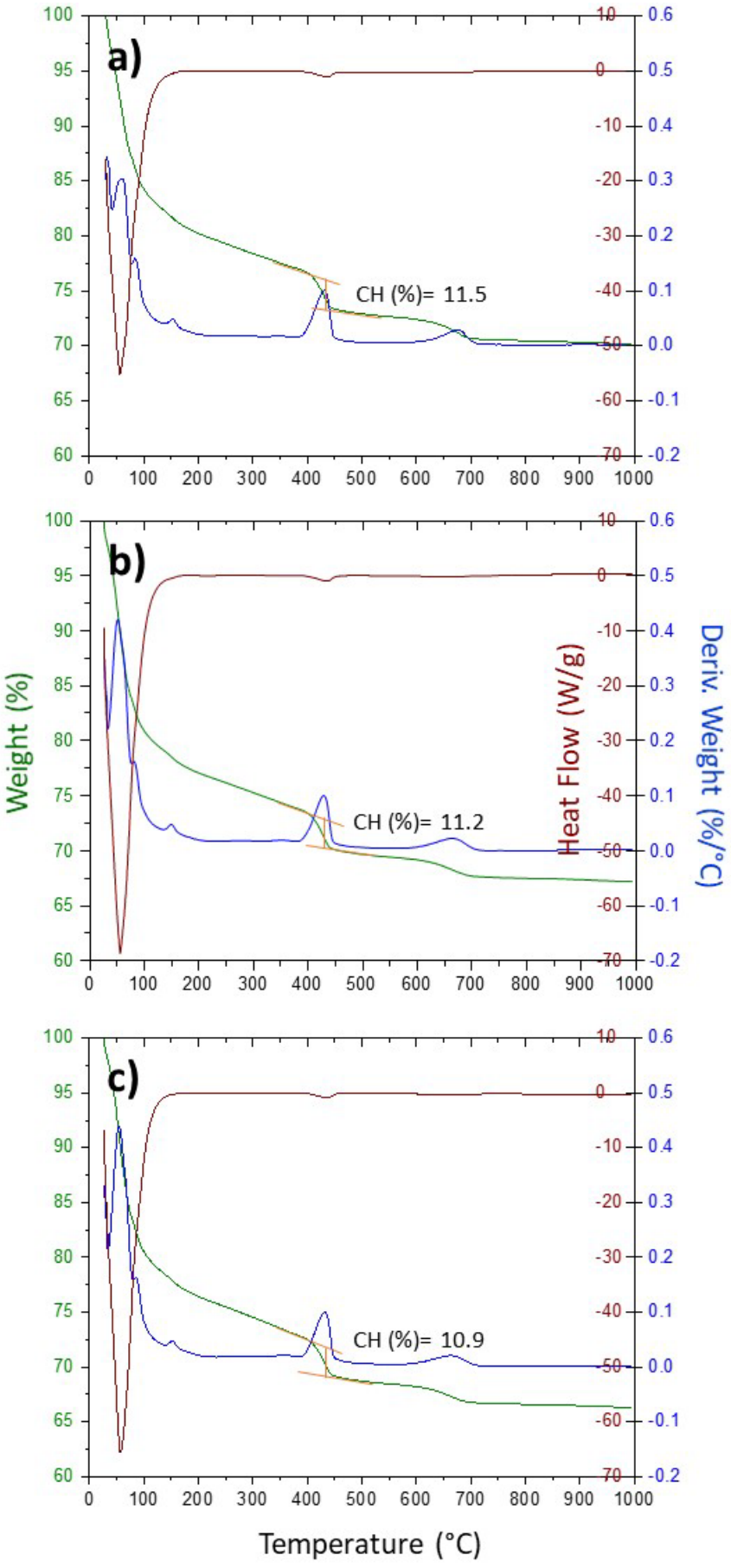

Figure S10. Thermal analysis traces for PC pastes (non-hydration arrested samples) with w/c=0.50, at 60ºC and at a) 2, b) 7, c) 28 days of hydration.

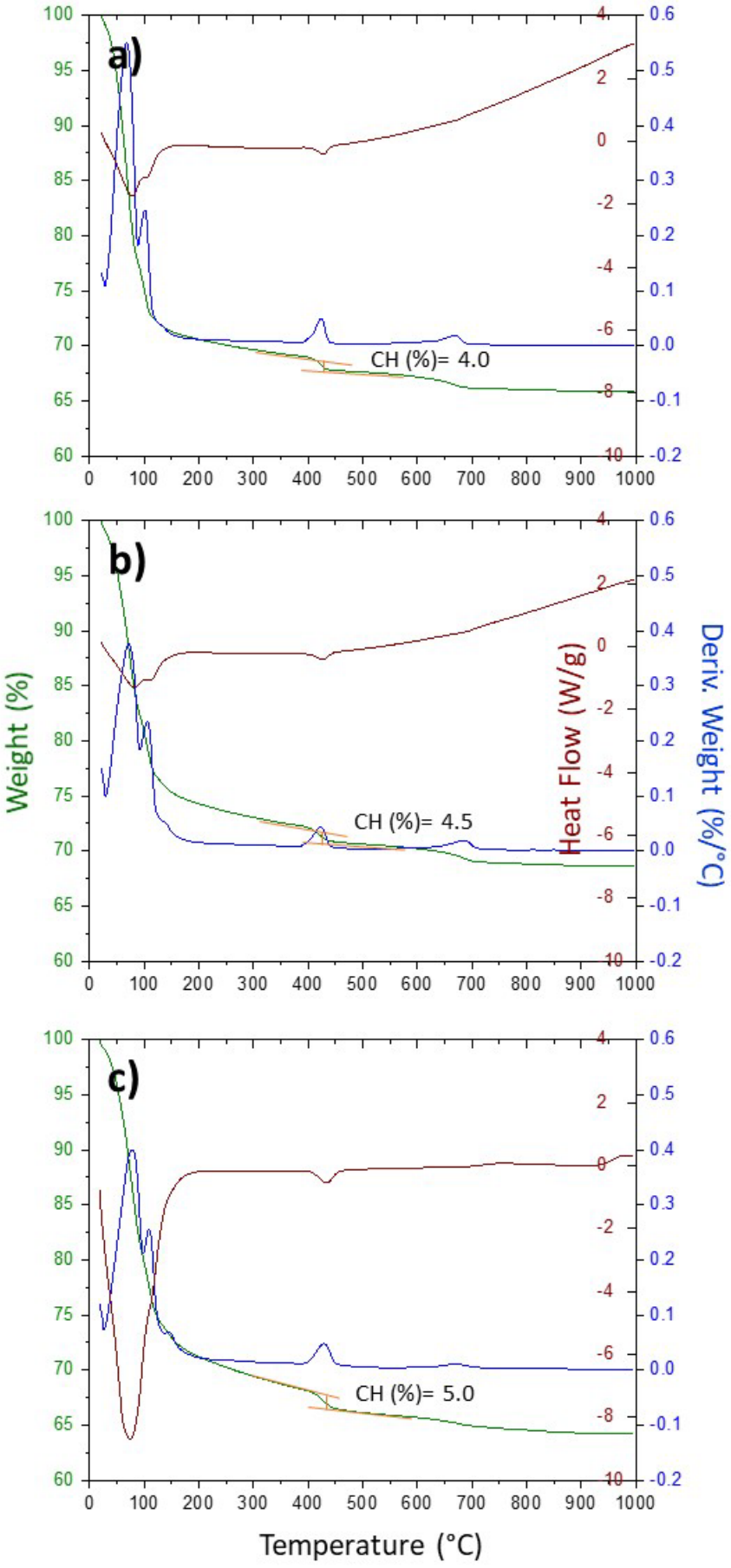

Figure S11. Thermal analysis traces for BC pastes (non-hydration arrested samples) with w/c=0.50, at 20ºC and at a) 3, b) 7, c) 28 days of hydration.

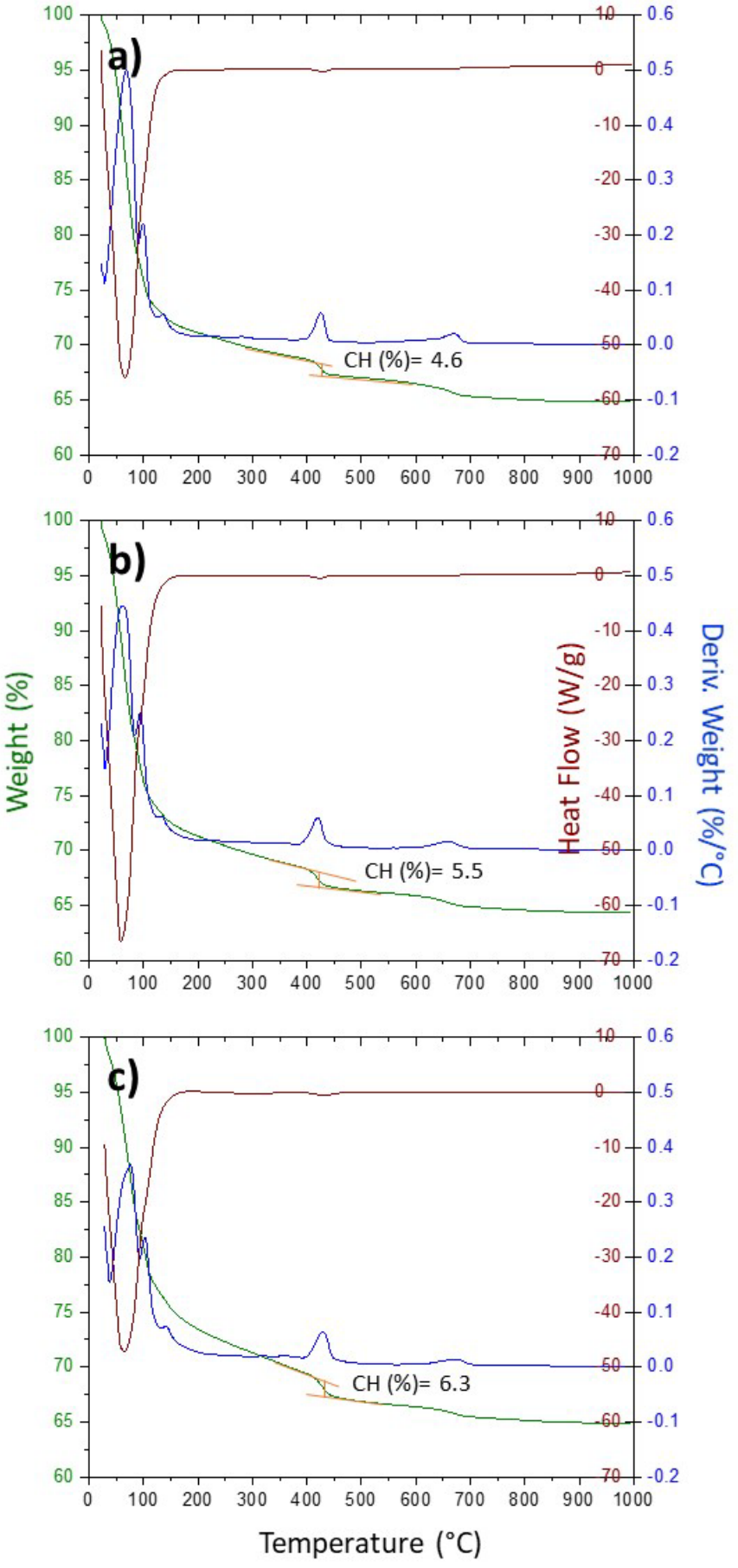

Figure S12. Thermal analysis traces for BC pastes (non-hydration arrested samples) with w/c=0.50, at 40ºC and at a) 2, b) 7, c) 28 days of hydration.

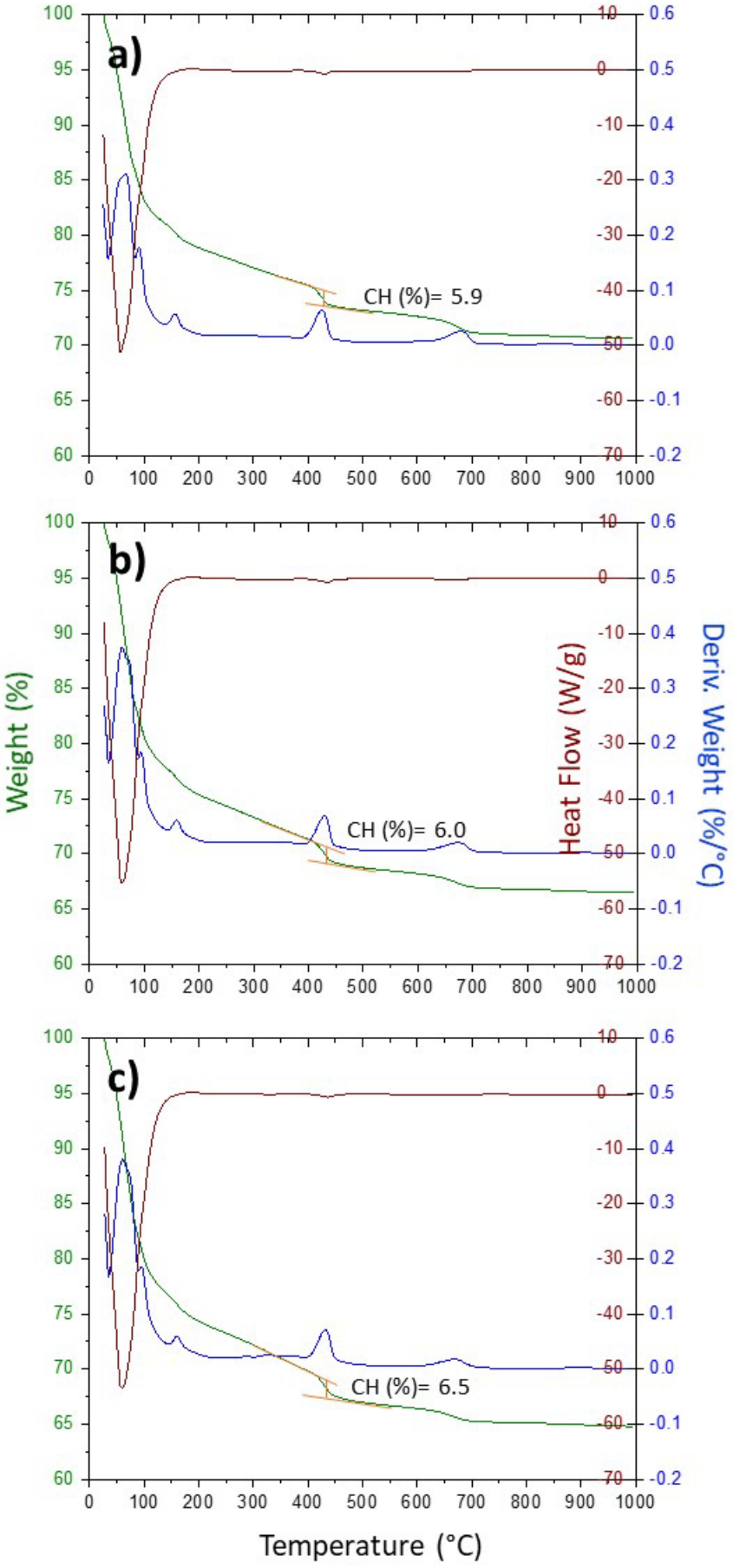

Figure S13. Thermal analysis traces for BC pastes (non-hydration arrested samples) with w/c=0.50, at 60ºC and at a) 2, b) 7, c) 28 days of hydration.

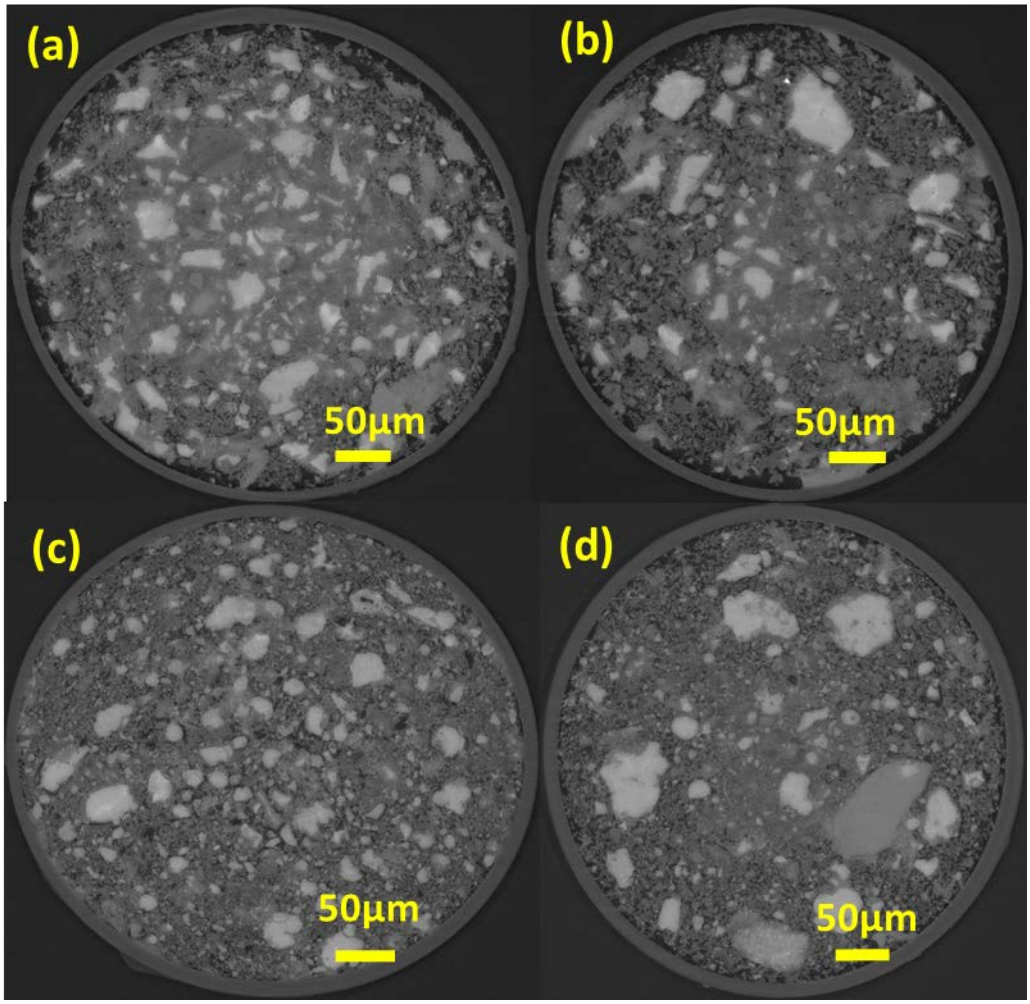

Figure S14. Paganin reconstructed orthoslices hydrated at 20ºC for (a) PC-3d-20ºC#11, (b) PC-7d-20ºC#12, (c) BC-3d-20ºC#18, and (d) BC-7d-20ºC#14.

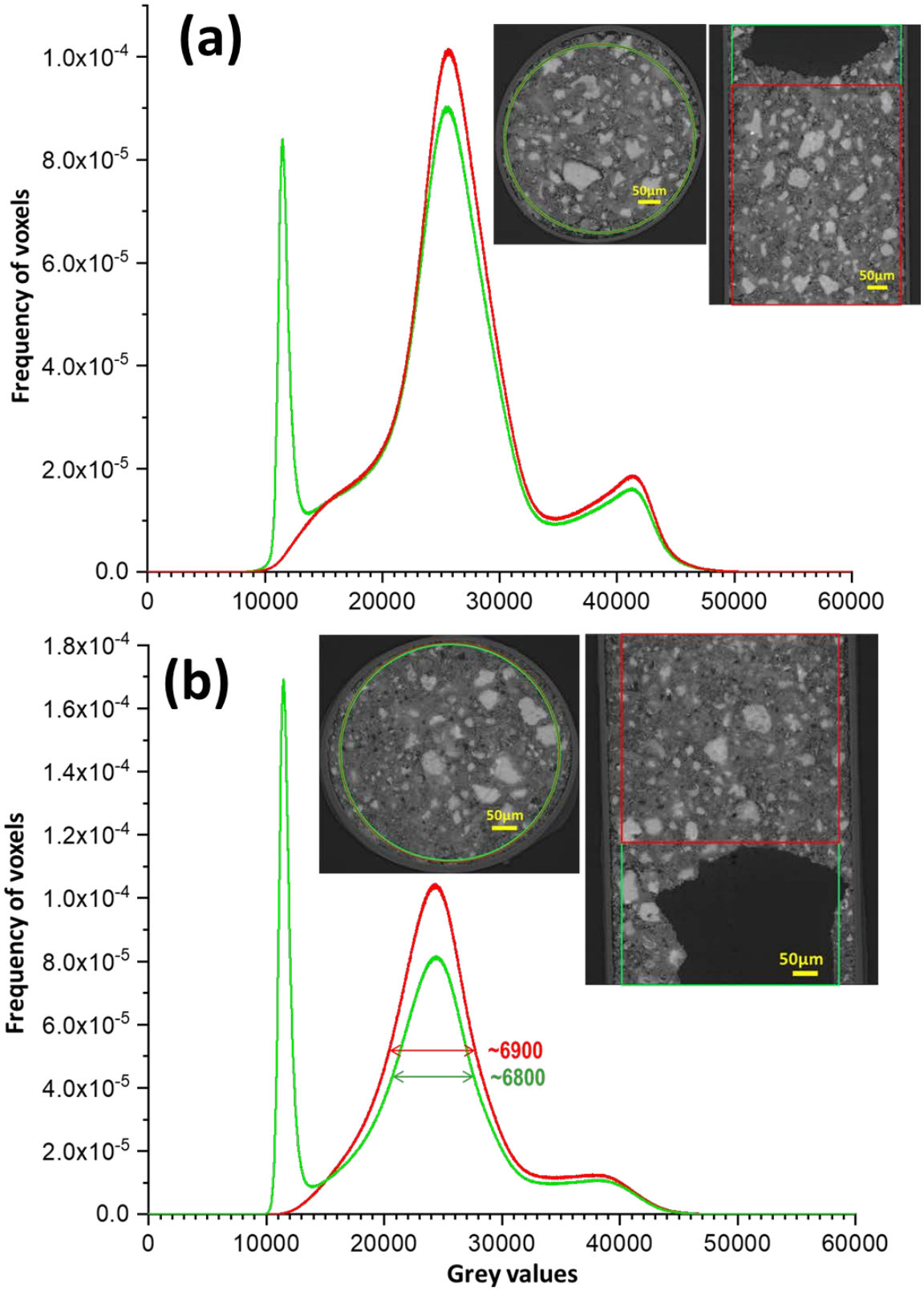

Figure S15. Volume of interest normalized grayscale histograms for (a) PC-28d-20ºC#13 and (b) BC-60ºC-28d#44, Paganin reconstructions, including (green traces) and excluding (red traces) the big pores. The insets show selected views to depict the cylindrical VOIs employed for these calculations. It is noted that the red VOIs do not contain the big air-filled pores and therefore their corresponding grayscale histograms do not show the sharp band centered at ~11000 grayscale value.

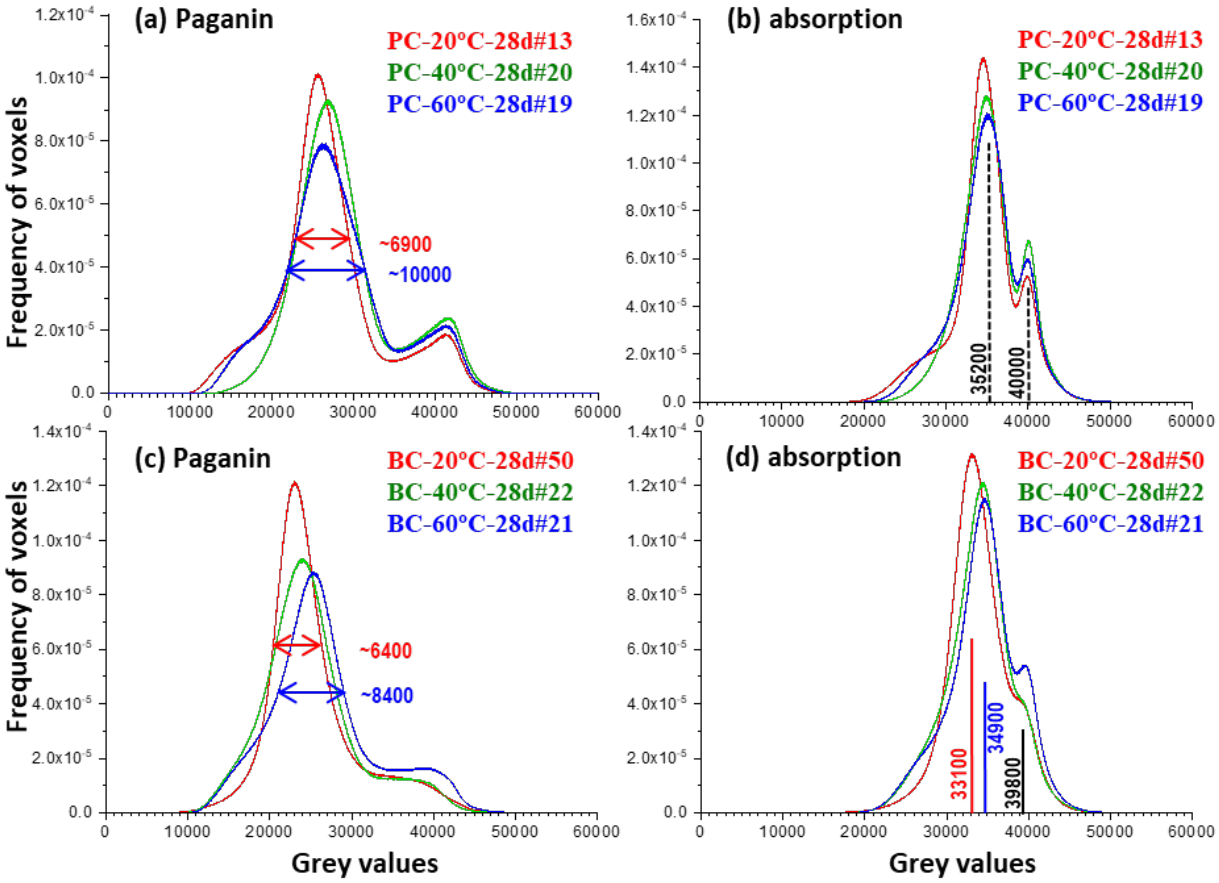

Figure S16. Volume of interest normalized grayscale histograms. (a) Paganin and (b) absorption traces for PC pastes with temperature at 28 days of hydration. (c) Paganin and (d) absorption traces for BC pastes with temperature at 28 days of hydration. Capillaries sealed by melting the tips. The big pore regions have not been included in the VOIs.

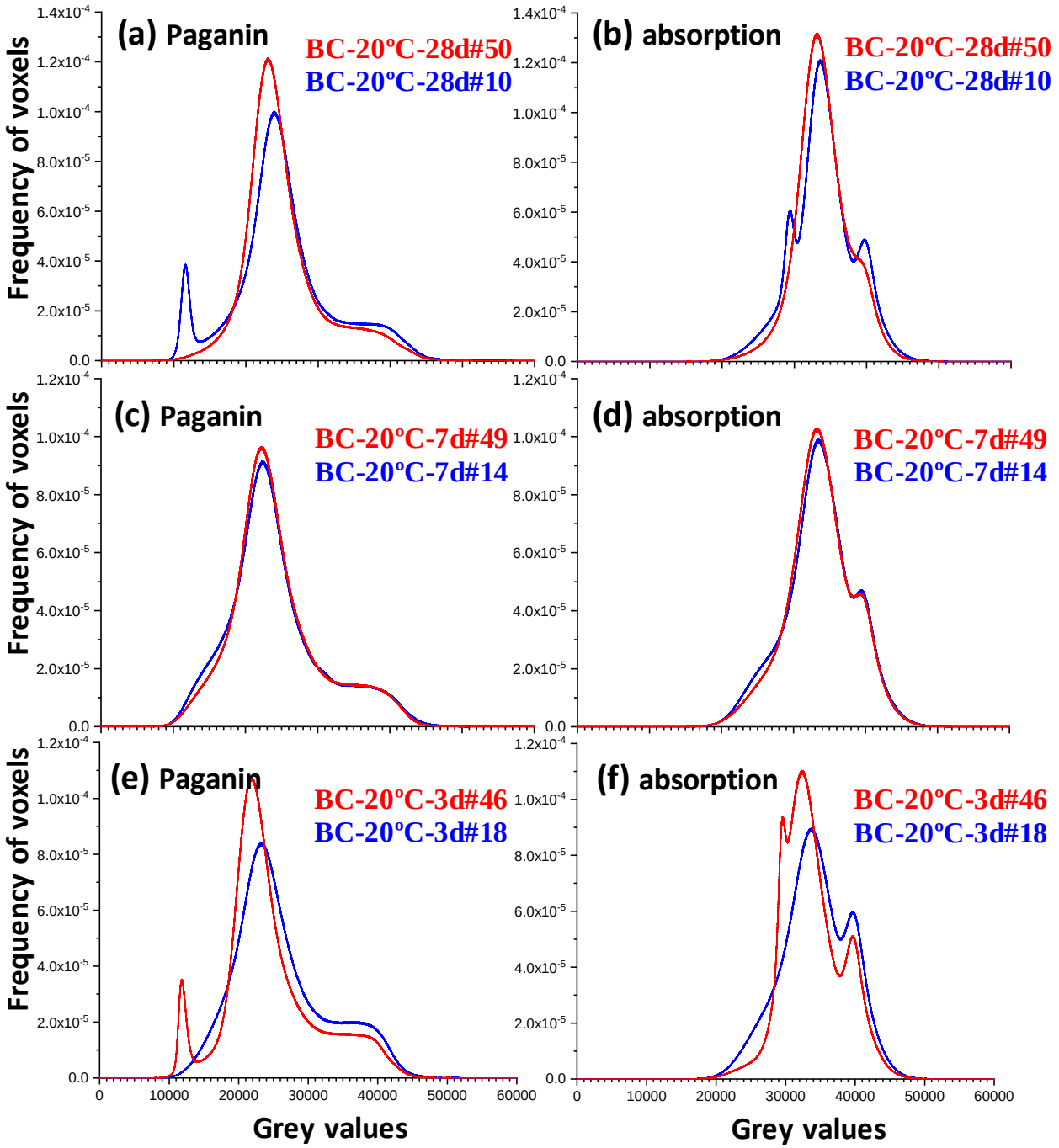

Figure S17. Volume of interest normalized grayscale histograms comparing repeats of different capillaries but filled with the same cement paste. (a) Paganin and (b) absorption traces for BC-20ºC-28d#50 and BC-20ºC-28d#10. (c) Paganin and (d) absorption traces for BC-20ºC-7d#14 and BC-20ºC-7d#49. (e) Paganin and (f) absorption traces for BC-20ºC-3d#18 and BC-20ºC-3d#46.

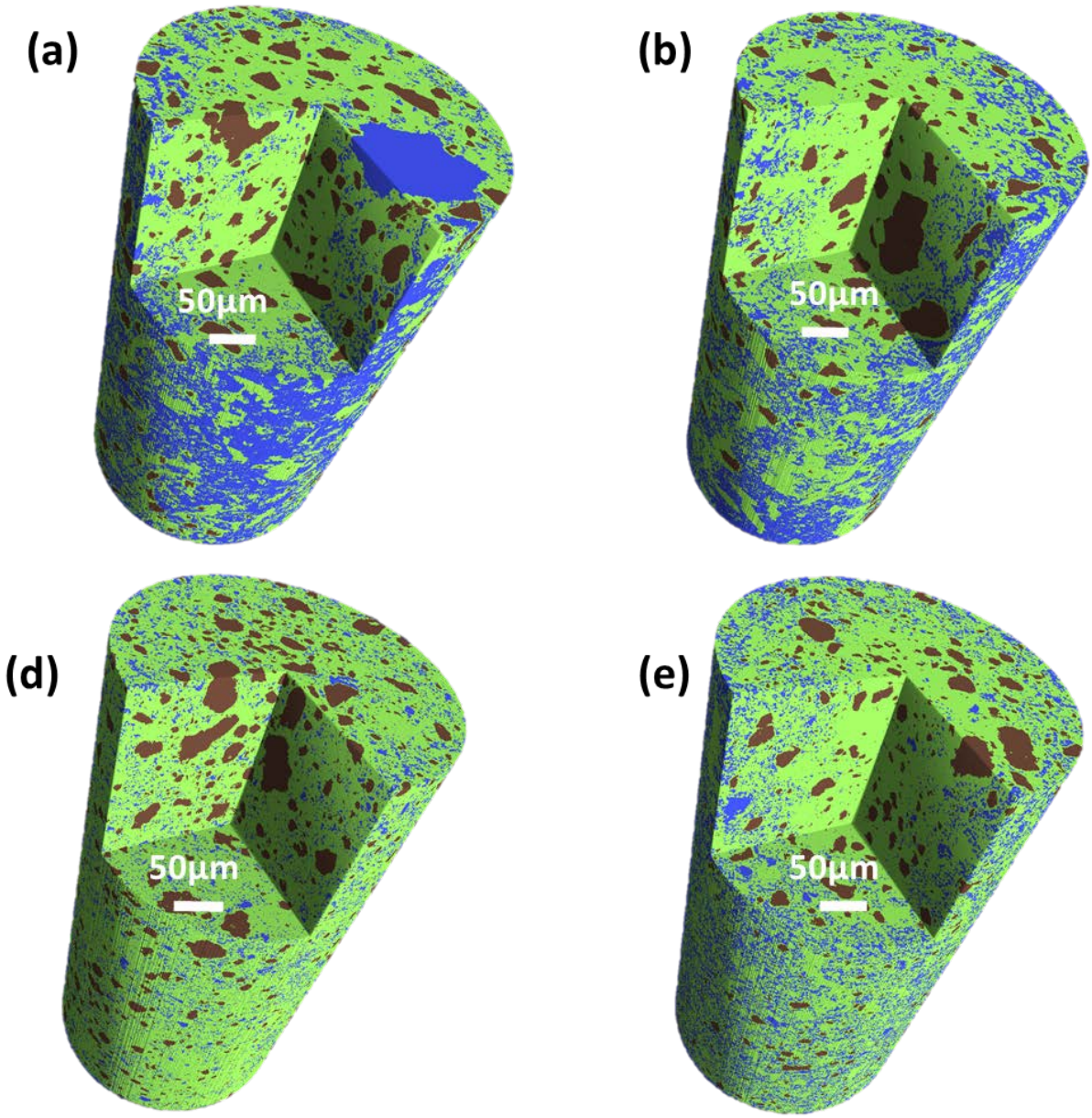

Figure S18. Rendered volumes displaying the results of the segmentations. Brown represents unhydrated cement components, green represents hydrated products and blue represents porosity (water and air). (a) PC-3d-20ºC-Pag#11, (b) PC-7d-20ºC-Pag#12, (c) BC-3d-20-ºC-Pag#18 and (d) BC-7d-20ºC-Pag#14.